

東京大学 大学院新領域創成科学研究科  
基盤科学研究系物質系専攻

平成29年度  
修士論文

Photoelectrochemical activity of co-doped  $\text{SrTiO}_3$   
共ドーピングしたチタン酸ストロンチウムの光触媒活性

2018年1月22日提出  
指導教員 リップマーミック 准教授 印

細川喜久

# Contents

|          |                                                                                       |           |
|----------|---------------------------------------------------------------------------------------|-----------|
| <b>1</b> | <b>Introduction</b>                                                                   | <b>2</b>  |
| 1.1      | Hydrogen society . . . . .                                                            | 2         |
| 1.2      | Water splitting with a photoelectrode . . . . .                                       | 4         |
| 1.3      | M:SrTiO <sub>3</sub> (M=Rh,Ir) epitaxial thin film photoelectrode for water splitting | 6         |
| 1.4      | Rh clustering in Rh:SrTiO <sub>3</sub> . . . . .                                      | 10        |
| 1.5      | Aim of this study . . . . .                                                           | 12        |
| <b>2</b> | <b>Method</b>                                                                         | <b>13</b> |
| 2.1      | Sample preparation . . . . .                                                          | 13        |
| 2.1.1    | Pulsed laser deposition . . . . .                                                     | 13        |
| 2.1.2    | Sample preparation process . . . . .                                                  | 17        |
| 2.2      | Reflection high-energy electron diffraction . . . . .                                 | 18        |
| 2.3      | Atomic Force Microscopy . . . . .                                                     | 20        |
| 2.4      | X-ray diffraction . . . . .                                                           | 21        |
| 2.5      | Optical absorbance measurement . . . . .                                              | 24        |
| 2.6      | X-ray photoelectron spectroscopy . . . . .                                            | 24        |
| 2.7      | Photoelectrochemical measurement . . . . .                                            | 26        |
| <b>3</b> | <b>Avoiding Rh clustering</b>                                                         | <b>31</b> |
| 3.1      | Optimizing Rh <sup>3+</sup> :SrTiO <sub>3</sub> growth . . . . .                      | 31        |
| 3.2      | Robust Rh valence in Rh <sup>3+</sup> :SrTiO <sub>3</sub> . . . . .                   | 32        |
| 3.3      | Optimizing Rh <sup>4+</sup> :SrTiO <sub>3</sub> stoichiometry . . . . .               | 35        |
| 3.4      | Reversible Rh valence . . . . .                                                       | 37        |
| <b>4</b> | <b>Rh valence control by La co-doping</b>                                             | <b>42</b> |
| 4.1      | Introduction . . . . .                                                                | 42        |
| 4.2      | Preparing a (La,Rh):SrTiO <sub>3</sub> ablation target . . . . .                      | 43        |

|          |                                                       |           |
|----------|-------------------------------------------------------|-----------|
| 4.3      | The effect of La,Rh co-doping on Rh valence . . . . . | 44        |
| <b>5</b> | <b>Photoelectrochemical activity</b>                  | <b>48</b> |
| <b>6</b> | <b>Conclusions</b>                                    | <b>54</b> |
|          | <b>References</b>                                     | <b>56</b> |
| <b>7</b> | <b>Acknowledgement</b>                                | <b>61</b> |

# Chapter 1

## Introduction

### 1.1 Hydrogen society

The population of the world is expected to increase from the current 7 billion to 9 billion by 2050 and to 10 billion by 2100. The International Energy Agency (IEA) estimates for the world energy demand an increase from 12 billion ton oil equivalents in 2009 to 17 ~ 18 billion tons in 2035. Fig. 1.1 shows the change of the shares of various energy sources used to cover the world energy needs. Fossil fuels cover most of the needs, with minor shares held by nuclear and hydroelectric power generation.

The use of nuclear fuels continues to have safety problems, as shown by the accident at Fukushima after the 2011 Tohoku earthquake. Meeting more strict safety requirements is likely to increase the deployment costs of nuclear energy, meaning that the nuclear power share cannot increase significantly. Hydroelectric power has a similar limitation, as it requires the construction of dams that require suitable water resources and also come with significant negative environmental impact. Increasing the number of hydropower stations cannot therefore meet increasing energy demands. An increase in the use of fossil fuels leads to an increase in carbon dioxide emissions. Carbon dioxide emissions are predicted by IEA to increase to ~ 40 gigaton in 2035 from 29 gigaton in 2009. Fossil fuel usage should thus be limited to avoid global climate change caused by increased carbon dioxide emissions. For continued development of civilization and to sustain a growing population, the amount of renewable energy supplies must increase. In practice, this means the use of solar energy in some form. While solar energy is clean and sustainable, the usage level remains low due to the difficulty of harvesting the very disperse flux of energy on the surface of the Earth.

One possible technology that is the subject of this thesis work, is solar water de-

composition in photoelectrochemical water splitting cells that produce hydrogen gas. Although solar cells are the most widely used solar energy harvesting devices, the use of sunlight in photoelectrochemical cells has a number of merits over solar cells. Solar cells are very good at harvesting solar energy but convert solar energy directly into electricity. Since it is difficult to store electricity efficiently, solar cell energy systems have limited use profiles. Photoelectrochemical cells, on the other hand, convert solar energy into hydrogen, which is a very attractive material as an energy resource. Hydrogen can be stored and transported, offering more flexible energy use than solar cells. By utilizing a fuel cell, hydrogen can be efficiently converted into electric current without emitting carbon dioxide.

Based on the benefits of hydrogen as an energy carrier, there is an idea to create a hydrogen society in Japan. However, at present, most of the industrial hydrogen is manufactured cheaply by steam reforming natural gas. However, in this method, methane is consumed and carbon dioxide is generated as a byproduct of hydrogen. On the other hand, water splitting in a photoelectrochemical cell only consumes water and sunlight without emitting carbon dioxide. Therefore, water splitting appears to be the preferred way to produce hydrogen, but unlike steam reforming, it has not been put to practical use due to the low efficiency of solar energy to hydrogen conversion. In order to solve this problem, the development of materials or structures for highly efficient photoelectrodes is necessary.

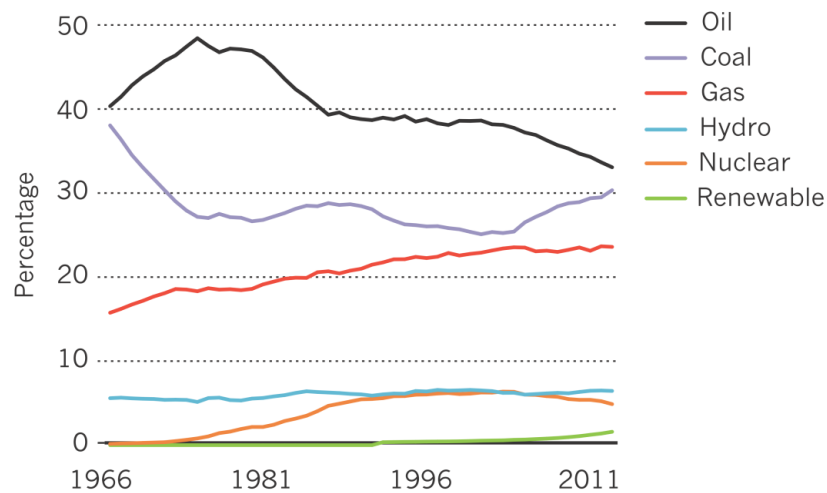


Figure 1.1: Shares of primary energy sources in the world from 1966 to 2011 [1].

## 1.2 Water splitting with a photoelectrode

Since Fujishima and Honda discovered photoelectrochemical water splitting using a rutile  $\text{TiO}_2$  single crystal electrode [2], numerous semiconductor based photoelectrode materials have been studied. Achieving practical photoelectrochemical water splitting would allow the production of hydrogen in a way that is environmentally sustainable, while the hydrogen is storable and transportable, similar to fossil fuels.

The principle of photoelectrochemical water splitting can be explained based on simple semiconductor theory. When a semiconductor photoelectrode is immersed in water, a space charge region forms, leading to band bending near the surface of the semiconductor. When the semiconductor is irradiated with light with a photon energy above the band gap, electron-hole pairs are generated by photoexcitation. If these carriers form in the band bending region, the charges are rapidly separated and either the holes or the electrons may reach the semiconductor surface along the internal field gradient and react with the electrolyte solution. In the case of a *p*-type semiconductor, the band bending is downward, and photoexcited electrons migrate to the surface. Charge balance in the cell is maintained by a current from a counter electrode, where the opposite reaction takes place. When the conduction band minimum of the *p*-type semiconductor is above the hydrogen generation potential, photoexcited electrons reaching the semiconductor surface can reduce water to hydrogen (Fig. 1.2a).

In the case of an *n*-type semiconductor, photoexcited holes are forced to the surface, following the potential gradient of upward band bending. When the valence band maximum is below the oxygen production potential, these holes can oxidize water to oxygen (Fig. 1.2b). Since the Fermi level of the opposing electrode coincides with the Fermi level of the *p*-type (*n*-type) semiconductor, if the Fermi level of the semiconductor is located lower (higher) than the oxygen (hydrogen) generating potential, holes (electron) at the surface of the counter electrode can oxidize (reduce) water to produce oxygen (hydrogen). Even when the Fermi level of the semiconductor is in a position unsuitable for the redox reaction of water, it is possible to drive the redox reaction by applying a voltage between the semiconductor and the counter electrode from outside. This is one advantage of a photoelectrode cell that is unavailable for a photocatalyst. Besides applying a voltage from the outside, by using a tandem structure, it is possible to overcome an undesirable band structure. When opposite polarity semiconductors are connected in place of the metal-counter electrodes, the carriers that reach the semiconductor counter electrode are photoexcited again to obtain a sufficient potential for the redox reaction. The tandem structure eliminates some of the limitations of semi-

conductors that can be used as photoelectrodes (Fig. 1.3). On the other hand, compared to one photoelectrode system, twice as many photons are required to split water for gaining the same amount of hydrogen.

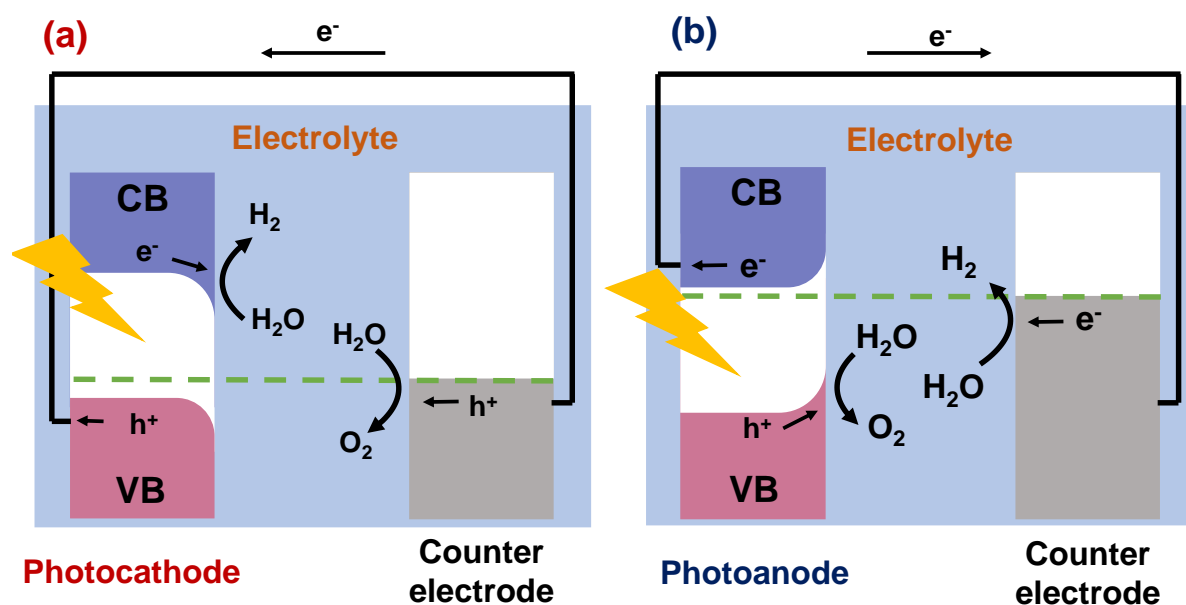


Figure 1.2: Water splitting reaction on (a) photocathode and (b) photoanode.

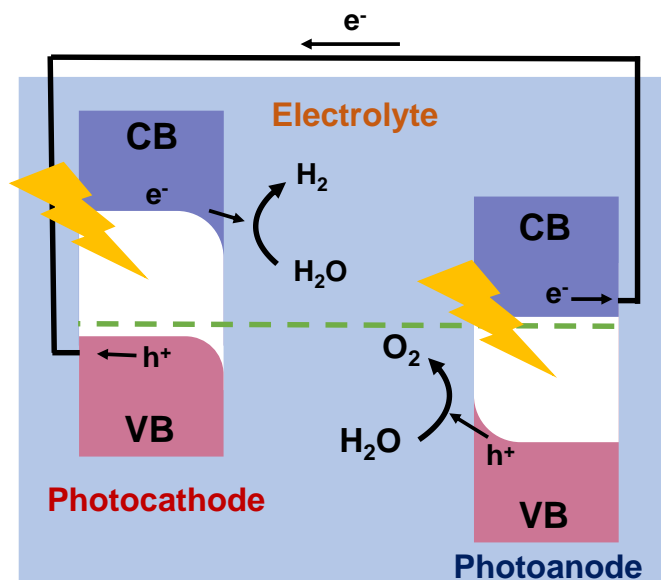


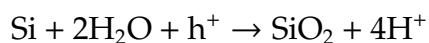
Figure 1.3: Tandem structure.

### 1.3 $\text{M:SrTiO}_3$ ( $\text{M}=\text{Rh}, \text{Ir}$ ) epitaxial thin film photoelectrode for water splitting

For a material to function as a photoelectrode in a photoelectrochemical cell, two important conditions must be satisfied. The first requirement is that the material must have a suitable electronic band structure for decomposing water. From the electrochemical point of view, in order to decompose water, either the energy of the conduction band minimum must be high enough relative to the reduction potential of water that photoexcited electrons can be injected from the semiconductor to water or the energy of the valence band maximum must be low enough for photogenerated holes to oxidize water. For the reaction to proceed, the band gap of the semiconductor must also exceed the 1.23 eV minimum required to decompose water. In practice, a slightly larger band gap of  $\sim 2$  eV is needed to provide a sufficient overpotential for either the reduction or oxidation process. Secondly, the photoelectrode needs to be stable in water during an electrochemical reaction. Silicon, for example, is the most widely used semiconductor for harvesting energy from sunlight, but it suffers from photocorrosion in an electrochemical reaction cell. In particular, for the water oxidation reaction, the



photogenerated holes tend to dissolve Si rather than split water. [3]. If Si is used in the electrolyte as a photoelectrode, the following reaction occurs due to photoexcited holes



The photoelectrode would thus be damaged by this reaction by photoexcited holes. This process is known as photocorrosion. It is indispensable for a photoelectrode to be stable against photocorrosion. An oxide semiconductor such as  $\text{TiO}_2$  [2], which is the material where photocatalytic water splitting activity was found for the first time, is a chemically stable semiconductor in photoelectrochemical reactions.

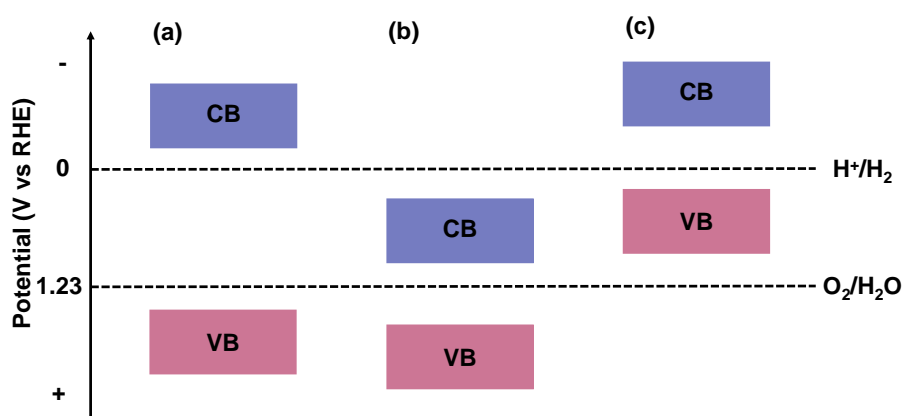


Figure 1.4: Redox potentials of water sandwiched between valence band and conduction band. (a) Band structure of a semiconductor capable of total water splitting, producing both oxygen and hydrogen. (b) Band structure capable of oxidation only. (c) Band structure capable of reduction only.

$\text{SrTiO}_3$  is another well-known water-stable oxide semiconductor material that can generate a photocurrent under irradiation with ultraviolet light. [4].  $\text{SrTiO}_3$  has been extensively studied and most of the fundamental physical properties are well known. The crystal structure is cubic perovskite with a lattice constant of  $3.905\text{\AA}$ . It is an indirect transition semiconductor with a band gap of  $3.2\text{ eV}$ . [5] The valence band and the conduction band completely sandwich the redox potentials of water [6], and it has all the necessary properties to be used as a photoelectrode.

However, due to the  $3.2\text{ eV}$  band gap,  $\text{SrTiO}_3$  can absorb only ultraviolet light. To efficiently convert sunlight into hydrogen, visible light should also be used. One strategy

for achieving visible light photoresponse in  $\text{SrTiO}_3$  is chemical doping. The dopant-related impurity states within the band gap effectively reduce the optical absorption edge energy.

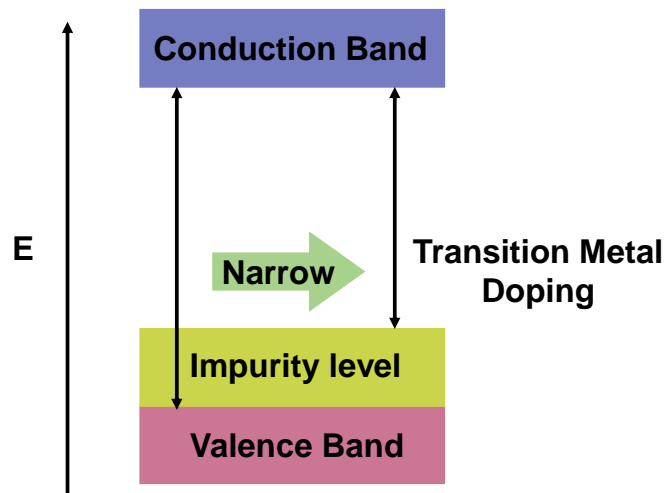


Figure 1.5: Schematic diagram of reducing the band gap by doping a wide-gap semiconductor. The band gap is narrowed by forming an impurity level within the band gap close to the valence band edge. Due to a narrower band gap, the doped material can absorb light of a larger wavelength range than the nondoped parent compound.

It is known that Rh-doped  $\text{SrTiO}_3$  shows photocatalytic hydrogen evolution activity under visible light [7] [6]. However, the photocatalytic activity of Rh: $\text{SrTiO}_3$  depends on the Rh valence state. Rh would normally be expected to substitute at the  $\text{Ti}^{4+}$ -site while the Rh valence of either  $\text{Rh}^{3+}$  or  $\text{Rh}^{4+}$  is determined by the presence of oxygen vacancies.  $\text{Rh}^{4+}$ : $\text{SrTiO}_3$  shows lower photoelectrochemical activity than  $\text{Rh}^{3+}$ : $\text{SrTiO}_3$ , because  $\text{Rh}^{4+}$ : $\text{SrTiO}_3$  has an unoccupied in-gap level caused by the  $\text{Rh}^{4+}$   $4d^5$  electronic configuration. The unoccupied mid-gap level promotes rapid trapping and recombination of photocarriers. It is thus necessary to stabilize the  $\text{Rh}^{3+}$  valence state to improve the energy harvesting efficiency.

Kawasaki et al. have succeeded in the fabrication of epitaxial Rh: $\text{SrTiO}_3$  photoelectrodes by PLD [8]. In that study, the Rh valence state was tuned by film growth conditions.  $\text{Rh}^{3+}$ : $\text{SrTiO}_3$  was grown in reducing conditions ( $700^\circ\text{C}$ ,  $10^{-6}$  Torr) and  $\text{Rh}^{4+}$ : $\text{SrTiO}_3$  in oxidizing conditions ( $700^\circ\text{C}$ ,  $10^{-1}$  Torr). Ir: $\text{SrTiO}_3$  is another possible photoelectrode material. [9] Photocatalytic activity of Ir: $\text{SrTiO}_3$  also depends on Ir

valence state.  $\text{Ir}^{4+}:\text{SrTiO}_3$  showed higher photocatalytic activity than  $\text{Ir}^{3+}:\text{SrTiO}_3$ . However,  $\text{Ir}:\text{SrTiO}_3$  is an *n*-type oxygen evolution photoanode material.  $\text{Rh}^{3+}:\text{SrTiO}_3$  is thus the most interesting *p*-type hydrogen evolution photocathode material with a suitable Rh 4*d* impurity level position close to the valence band maximum as illustrated in Fig. 1.5.

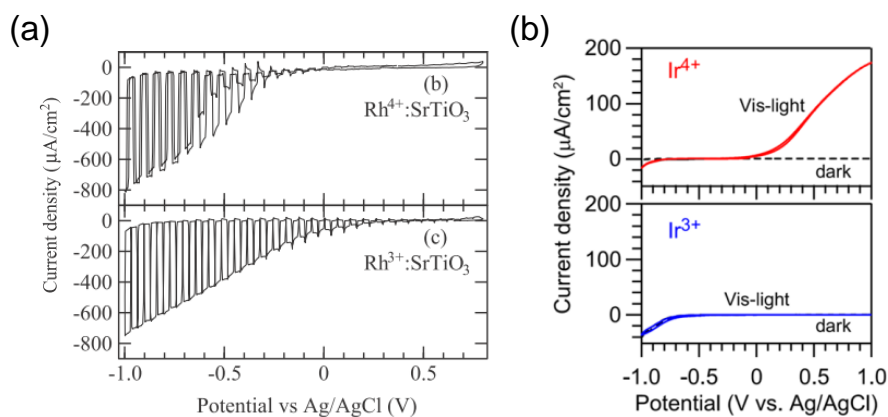


Figure 1.6: Cyclic voltammogram of (a) $\text{Rh}:\text{SrTiO}_3$  and (b) $\text{Ir}:\text{SrTiO}_3$  under visible light.  $\text{Rh}^{3+/4+}:\text{SrTiO}_3$  showed photocathodic behavior (produces hydrogen gas) while  $\text{Ir}^{3+/4+}:\text{SrTiO}_3$  works as a photoanode (produces oxygen gas).  $\text{Rh}^{4+}:\text{SrTiO}_3$  shows hysteretic behavior related to the reduction of  $\text{Rh}^{4+}$  ions to  $\text{Rh}^{3+}$ . [8,9]

## 1.4 Rh clustering in Rh:SrTiO<sub>3</sub>

The valence state of Rh in SrTiO<sub>3</sub> can be easily determined visually by color of the sample, with Rh<sup>3+</sup>:SrTiO<sub>3</sub> being bright yellow while Rh<sup>4+</sup>:SrTiO<sub>3</sub> is dark purple. In Rh:SrTiO<sub>3</sub> samples where the Rh valence is determined by the presence of oxygen vacancies, it should thus be easy to observe the valence change in reducing or oxidizing annealing procedures by looking at the color of a thin film sample.

The color shift phenomenon is already known from bulk powder materials and is not unique for thin films. However, in earlier thin film work, Rh<sup>3+</sup>:STO samples grown at 10<sup>-6</sup> Torr were yellow as expected, but the film color appeared to be determined purely by the growth conditions and didn't change after post-annealing at 500°C in air [8]. The lack of a color change shows that the Rh valence state did not change although the crystal was annealed at conditions that would normally fully oxidize SrTiO<sub>3</sub>. This behavior is caused by the formation of dopant clusters where an oxygen vacancy is combined with one or two Rh atoms. Since each oxygen vacancy effectively donates two electrons into the SrTiO<sub>3</sub> crystal, a single vacancy can convert two Rh<sup>4+</sup> cations to the Rh<sup>3+</sup> state. These clusters are stable even in oxidizing annealing conditions because cation diffusion does not occur in the oxide crystal at 500°C. For this reason, it may be impossible to reversibly change the Rh valence in films grown under reducing conditions. At the same time, the lack of valence reversibility is a simple indicator of defect cluster formation, which is undesirable from the point of view of photocarrier trap center formation.

The formation of dopant clusters may be affected by the cation stoichiometry of a SrTiO<sub>3</sub> crystal. A deviation of the Sr/Ti ratio from the ideal 1:1 stoichiometry would lead to either Sr vacancies under Ti-rich conditions or to the formation of SrO rocksalt defects under Sr-rich conditions. In the PLD process, slight, percent-order stoichiometry adjustments can be done by tuning the ablation laser fluence. The effects of laser fluence stoichiometry tuning have been studied for metallic Nb:SrTiO<sub>3</sub>, where the presence of Sr vacancies or SrO rocksalt layers rapidly decrease the carrier mobility and the carrier number. When the laser fluence is too high, Sr vacancy clusters may form [11]. For too low fluence, additional SrO layers may grow. Onishi et al. achieved stoichiometric low-defect Nb:SrTiO<sub>3</sub> films by optimizing the laser fluence [10]. The results of this work are illustrated in Fig. 1.7, which shows the TEM images of stoichiometric and non-stoichiometric films, and in Fig. 1.8, showing the effect of laser fluence on the measured lattice parameter of the SrTiO<sub>3</sub> films. Based on this result, it is possible that the formation of Rh dopant clusters in Rh<sup>3+</sup>:SrTiO<sub>3</sub> can also be controlled by fine-tuning

the ablation laser fluence during film growth.

Besides the stoichiometry control by laser fluence, the film growth temperature has a major effect on the defect structure of a thin film. It has been reported, based on first-principles calculations, that Sr partial Schottky-type defects can be generated more easily than Ti partial Schottky-type defects in  $\text{SrTiO}_3$  [13]. Kozuka et al. overcame the defect problem in  $\text{SrTiO}_3$  thin films by increasing the PLD process temperature and found the optimum growth temperature to be close to  $1200^\circ\text{C}$ . [12] However, the same strategy cannot be used for  $\text{Rh:SrTiO}_3$  due to the relatively high vapor pressure of  $\text{Rh}_2\text{O}_3$  which will easily evaporate in a low-pressure process at high temperatures. For this reason,  $\text{Rh:SrTiO}_3$  films have to be grown at a relatively low temperature of  $700^\circ\text{C}$ , which is well below the optimal  $\text{SrTiO}_3$  film growth temperature of over  $1000^\circ\text{C}$ . The results of X-ray photoelectron spectroscopy support this conclusion. The Rh content detected by XPS in  $\text{Rh:SrTiO}_3$  films grown at  $1100^\circ\text{C}$ ,  $10^{-6}$  Torr was nearly zero. [8]

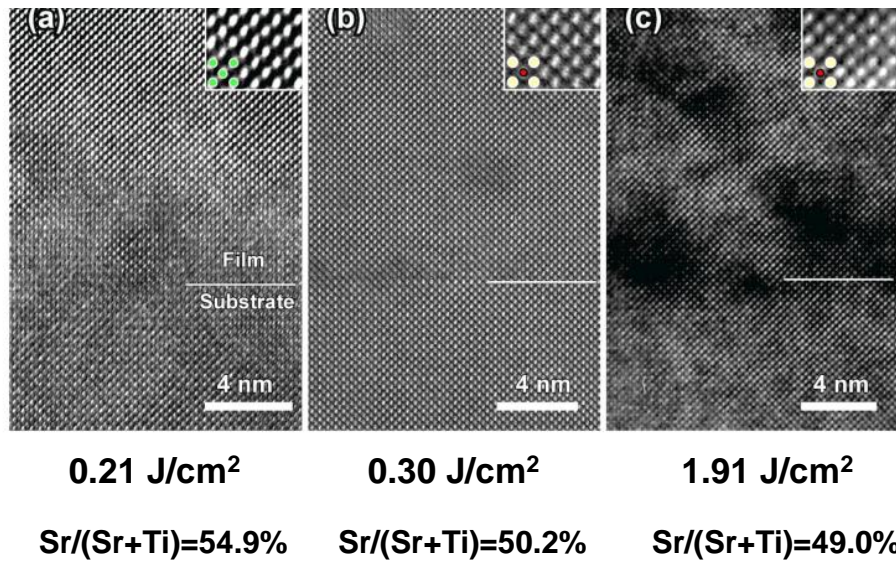


Figure 1.7: Cross-sectional transmission electron microscope (TEM) images of homoepitaxial  $\text{Nb:SrTiO}_3$  films on  $\text{SrTiO}_3$  substrate grown at various laser fluences. The insets show  $4 \times 4$  unit cells. The cation ratio of films was measured with in situ energy dispersive x-ray spectroscopy (EDS). The  $c$ -axis expansion of the three samples was (a) 0.129, (b) 0.004, and (c) 0.050 Å. Lower laser fluence induced Ruddlesden-Popper-type lattice defects associated with SrO extra layers, while higher laser fluence generated Sr vacancies. Based on these result, the presence of lattice defects can be indirectly detected by lattice expansion measurement. [10]

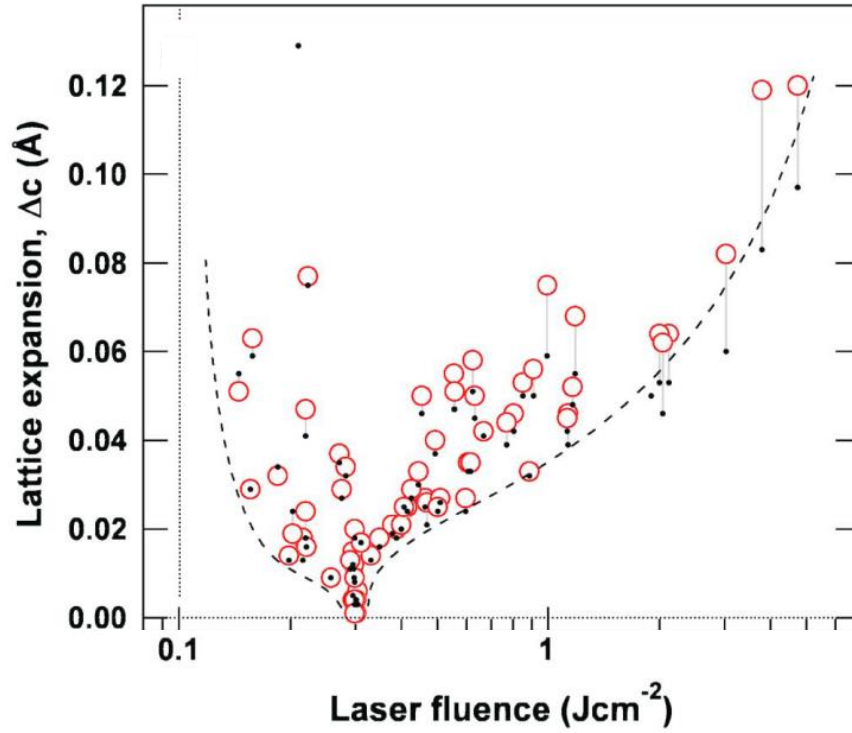


Figure 1.8: Lattice expansion of Nb:SrTiO<sub>3</sub> films as a function of laser fluence. The lattice constant changed systematically. [10]

## 1.5 Aim of this study

The aim of this study is to stabilize the Rh<sup>3+</sup> state in Rh:SrTiO<sub>3</sub> thin film photocathodes with low cation defect density and to demonstrate an enhancement of photoelectrochemical activity in a photoelectrode that does not contain anion or cation-anion defect clusters.

# Chapter 2

## Method

### 2.1 Sample preparation

#### 2.1.1 Pulsed laser deposition

The thin film samples used in this study were all grown by pulsed laser deposition (PLD). PLD is one of the physical vapor deposition methods for thin films where a laser is used to vaporize a solid target. Other well-known physical vapor deposition techniques are sputtering and molecular beam epitaxy (MBE). Each deposition technique has specific advantages and limitations. One of the main reasons for using PLD for oxide thin film growth is that PLD can be used to grow thin films over a wide range of background gas pressures. The background gas is usually pure oxygen and the process pressure may vary from  $10^{-8}$  Torr to 1 Torr. MBE can only be used to grow thin films in high vacuum conditions, typically at background pressures of less than  $10^{-6}$  Torr. Reactive gases, such as oxygen radicals or ozone must therefore be used to oxidize the film. Sputtering introduces inert gas into the process chamber and can thus be used at pressures above about  $10^{-4}$  Torr. On the other hand, in PLD, the pressure limits are very broad, which makes it possible to choose the best pressure range to obtain the desired oxide phase.

The second reason to use PLD is the ability to grow complex oxide phases that may contain three or more different cations. Since the transfer of material from a target to the film is nearly stoichiometric, it is often easier to obtain complex oxide phases by PLD than by sputtering or MBE.

The third main reason is the ability to control the film thickness with submonolayer accuracy by using in-situ diagnostic tools, such as reflection high-energy electron diffraction. This option is generally not available in sputter deposition.

PLD also has various limitations. The laser ablation plume is small, which means that the film growth rate is homogeneous only over a small area of less than 10 mm, reducing the maximum usable substrate size. Available substrate sizes are much larger for MBE and especially for sputtering, which is often used as an industrial film growth technique. PLD films also tend to have higher point defect densities than the best MBE-grown crystals.

Figure 2.1 shows a schematic illustration of the PLD chamber used in this study. The oxygen vacancy density and the precise cation stoichiometry are important parameters for the doped semiconductor films studied in this thesis work. The vacancy density and the cation ratio of a thin film grown by PLD depend on the oxygen background pressure, the laser fluence, the substrate temperature, and the film growth rate. For that reason, a chamber that can cover a wide range of process conditions is needed. The oxygen gas pressures that can be used in this particular PLD chamber range from  $10^{-9}$  Torr (base pressure) to  $\sim 1$  Torr. A pulsed KrF excimer laser (Lambda Physik COMPex 201) was used to ablate the sintered ceramic target pellets. By using a focus lens and an optical attenuator, it was possible to adjust the laser fluences by changing either the total incident laser pulse energy or the size of the laser focus area on the target surface. During thin film growth, the substrate temperature was monitored with an optical pyrometer (FTC, Japan Sensor) operating at around  $2\text{ }\mu\text{m}$  wavelength while the sample was heated with a Nd:YAG laser (SL117C, NEC) operating at a wavelength of  $1.064\text{ }\mu\text{m}$ . This ensured uniform substrate temperatures with a maximum process temperature of  $1400^{\circ}\text{C}$  and controlled temperature ramping under feedback control from the pyrometer. A view of the deposition system is shown in Figure 2.2.



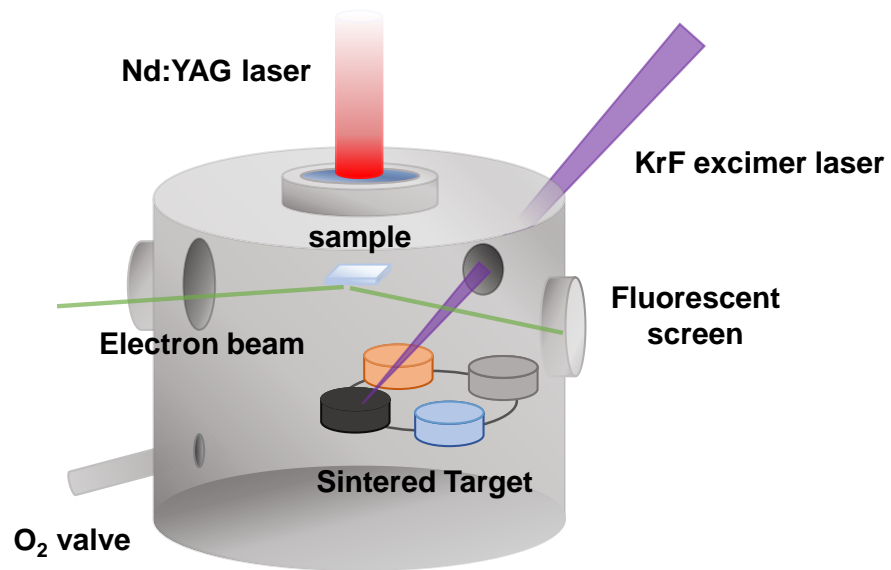


Figure 2.1: Schematic illustration of Pulsed laser deposition chamber.

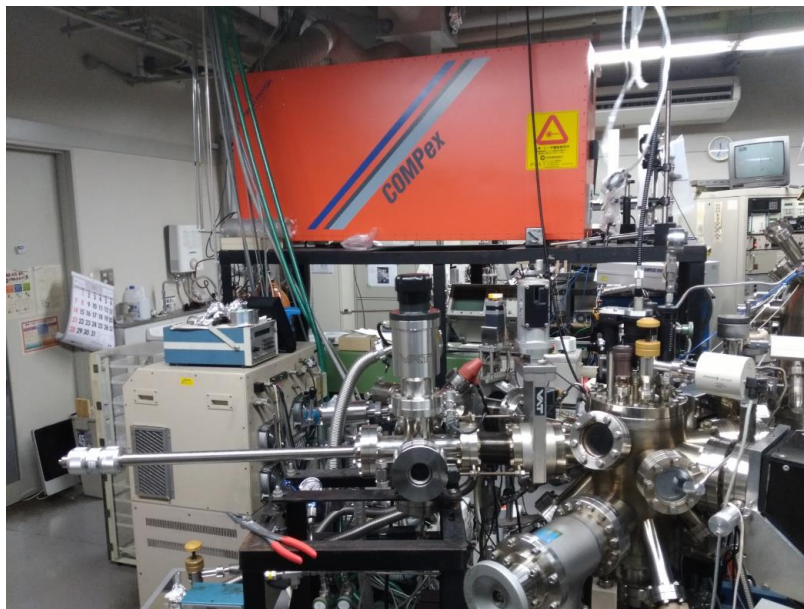


Figure 2.2: A picture of the deposition chamber and the COMpex excimer laser.

Since Nd:YAG laser operates in the near-infrared range, most typical oxide substrates are transparent for the laser light and cannot absorb the heating laser light.

Therefore, it is necessary to arrange another material on the back side of the substrate to absorb the infrared light of the Nd:YAG laser and transfer the heat to the substrate. Figure 2.3 shows a schematic diagram of the sample holder. This folder had a square hole at the center for constructing a heat conduction system. As a layer for absorbing heat, a 200  $\mu\text{m}$  Ni sheet (Nilaco) was oxidized in an electric furnace and mounted on a sapphire spacer. The sapphire sheet provided mechanical support and also thermal insulation from the main frame of the sample stage. To obtain uniform thermal contact between a substrate and the Ni heat absorber, a 5  $\mu\text{m}$  Ni foil (Nilaco) was inserted between the heat susceptor and the substrate. This sheet becomes soft at the working temperature and improves the heat contact and uniformity while still being easy to remove after deposition without contaminating the substrate, as happens when silver or platinum pastes are used. The whole substrate, heat absorber, and sapphire support sandwich was clamped with two stainless steel clamps from two edges, leaving the center part of the substrate accessible for surface analysis by reflection high-energy electron diffraction (RHEED).

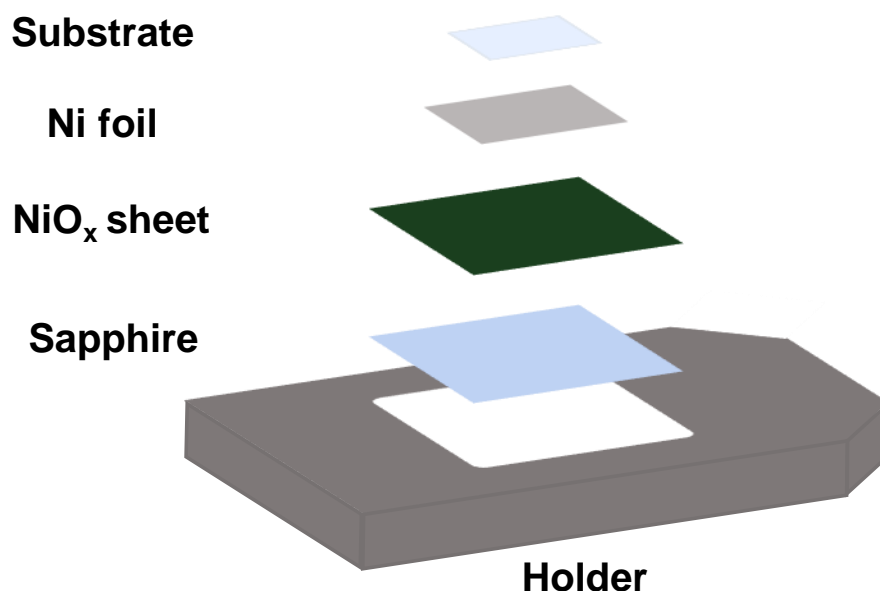


Figure 2.3: Sample holder used in the chamber. A Substrate and insert was attached to the holder with stainless steel clamps.

### 2.1.2 Sample preparation process

All thin films were grown by PLD. Fig. 2.4 shows the typical film growth schedule in this thesis. The as-supplied substrates were washed into acetone for 10min under ultrasonic agitation to eliminate surface contamination before it was used. After single crystal substrates were loaded into deposition chamber, these substrates were pre annealed under 900°C for 10min at  $10^{-5}$  Torr to realize atomic step-terrace structures and to remove contaminations on the surface. Subsequently, films were grown with various conditions. Some of these films were annealed in following two conditions. One is under 400°C for 6 hours in air to fill oxygen vacancy. This annealing process is carried out in many oxide thin film studies. This annealing process is called as “post-anneal or post-annealing” in this thesis. The other condition is under 800°C for 3hours at  $10^{-6}$  Torr. In this reductive condition, many oxygen vacancies is formed

in thin film. Often, the formations of vacancies are undesirable in the oxide thin film studies, however, intentionally introduced in this study to reduce Rh. This annealing is called “ vacuum-anneal or vacuum-annealing ” in this thesis.

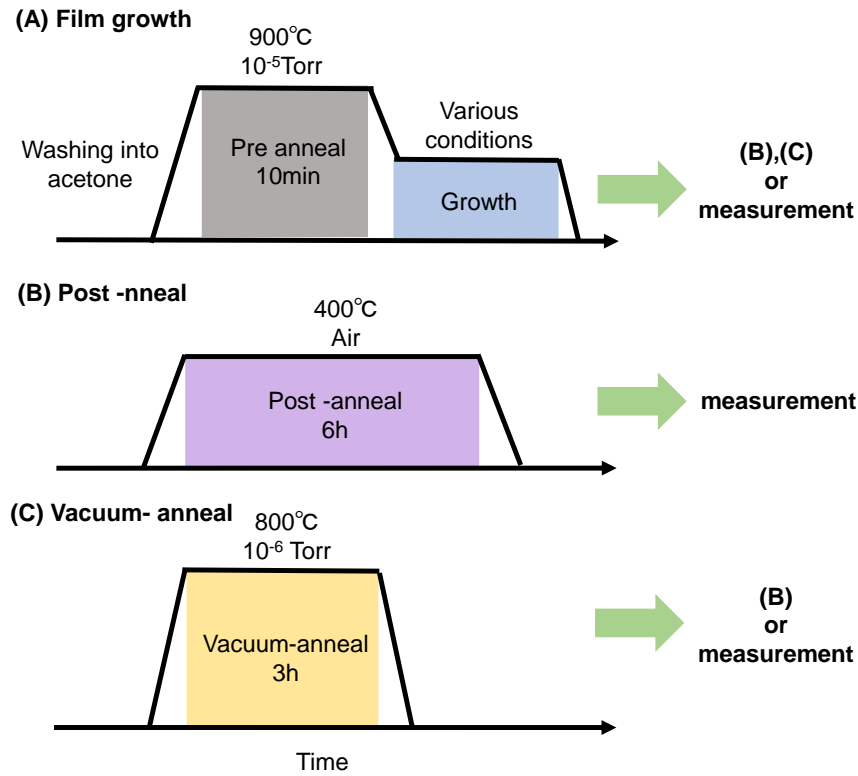


Figure 2.4: Sample preparation schedule. Post-annealing was done into electric furnace. Vacuum-annealing was performed into deposition chamber by Nd:YAG heating laser.

## 2.2 Reflection high-energy electron diffraction

Reflection high-energy electron diffraction (RHEED) is a tool used for controlling thin film growth in-situ and at the atomic level. In an RHEED measurement, the surface of the sample is irradiated with a high-energy electron beam and the reflected or diffracted electrons are detected on a fluorescent screen. The acceleration voltage of the electron gun was usually 25 kV and the grazing angle of the irradiated electron beam was set between  $0.5^{\circ}$  and  $2.5^{\circ}$ . The diffraction pattern corresponds to the two-dimensional reciprocal lattice space projected on the fluorescent screen containing information on the surface of the sample. Due to the low grazing incidence angle, the technique is

very surface sensitive and it is therefore possible to obtain information on the surface structure and surface roughness of a thin film in-situ and in real time. Figure 2.5 shows some typical surface structures and the corresponding reciprocal space and RHEED patterns.

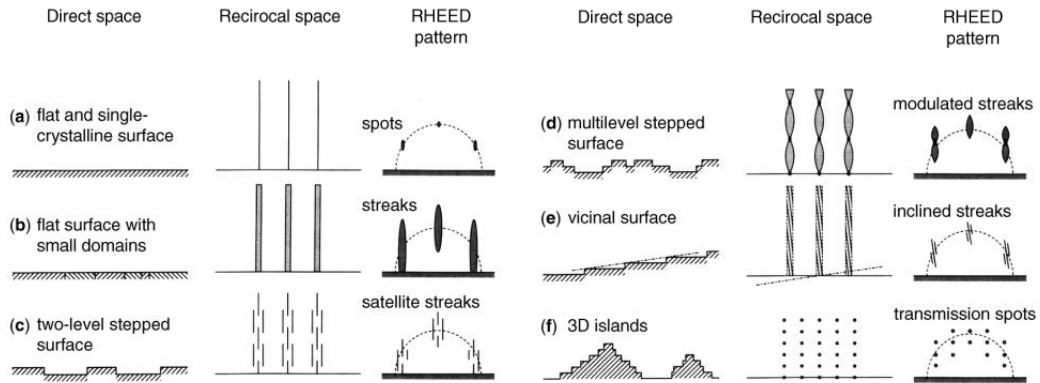


Figure 2.5: Typical RHEED patterns that can be observed for different surface structures. [14]

During film growth, RHEED observation makes it possible to monitor the growth dynamics of the thin film. The intensity of the electron beam that is reflected from the surface depends on the atomic-scale flatness of the surface. When adatoms are deposited on an atomically flat terrace and islands start to nucleate, the electron scattering increases and the observed specular RHEED intensity decreases accordingly. When the mobility of adatoms is small, the surface will quickly develop larger three-dimensional clusters and a flat surface cannot be recovered. In this case, the RHEED intensity decreases rapidly and does not recover. This crystal growth mode is called 3D growth.

On the other hand, if the temperature is high enough, the growth rate low enough, or the adsorbed atoms have sufficient energy to move to a stable crystallization site, the surface roughness can vary periodically as new layers are nucleated and gradually filled on the surface. The observed RHEED specular intensity follows these roughness changes. If the surface mobility of atoms is sufficient for a flat surface to be recovered after every deposition pulse, a sudden decrease of RHEED intensity is followed by exponential recovery for each pulse. This is due to the fact that the adsorbed atoms attach to existing step edges on the surface without changing the average step density.

This growth mode is called step-flow growth. Step-flow growth can only be observed on vicinal surfaces at sufficiently substrate temperature and for slow deposition rates. Pure step-flow growth in  $\text{SrTiO}_3$  has been observed for homoepitaxial growth at  $10^{-6}$  Torr oxygen pressure, at a growth temperature of over  $1000^\circ\text{C}$  at a PLD pulse rate of 0.2 Hz [15].

In an intermediate case, atomic layers nucleate and fill periodically even when the surface recovery is not complete after each deposition pulse. In this case, the RHEED intensity shows periodic oscillations that correspond to the growth of individual unit cell layers. This film growth mode is called layer-by-layer growth. By using this growth mode, it is possible to know the number of deposition pulses required for growing one unit cell layer. This makes it possible to control the film thickness with an accuracy of one unit cell.

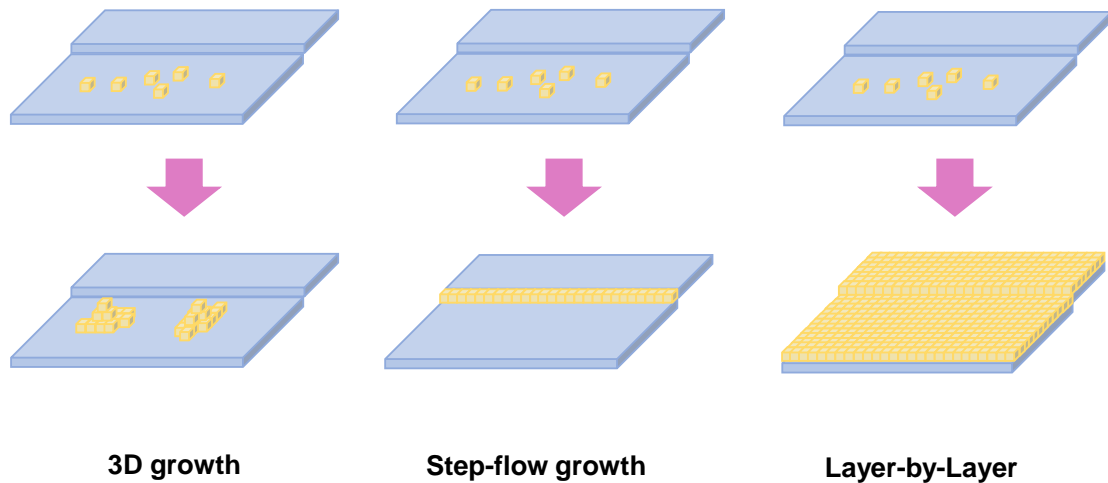


Figure 2.6: Illustration of typical thin film growth modes.

## 2.3 Atomic Force Microscopy

The surface morphology of thin films was observed with a Shimadzu SPM-9600 atomic force microscope (AFM). Since AFM does not require ultrahigh vacuum or special surface treatment for measurement, the surface structures can be easily observed. In this work, contact mode and non-contact imaging modes were used. In the contact mode, the AFM image is formed by measuring the deflection of a cantilever that is in

contact with the sample surface. The cantilever deflection is detected with a photodiode that measures the movement of a laser beam reflected from the tip of the cantilever. A constant cantilever deflection is maintained by a feedback loop and a calibrated piezoelectric sample positioning stage. The surface topography imaging is performed using the correction voltage applied by the feedback loop to the piezoelectric stage.

In the non-contact mode, the surface of the sample is scanned while the cantilever vibrates at its resonance frequency close to the sample surface. Again, the image is formed with the help of a feedback signal that maintains a constant vibration frequency of the tip. At the time of measurement, a vibration isolation system (TS - 150, Table Stable Ltd.) was placed under the AFM to reduce external mechanical vibrations (Fig. 2.7).

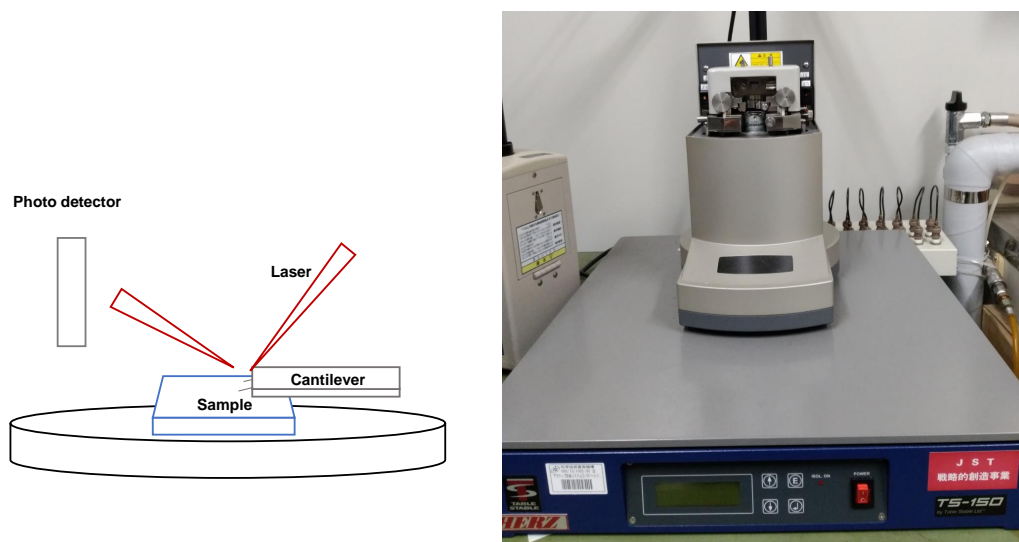


Figure 2.7: Left: Schematic illustration of the operation of an atomic force microscope. Right: Shimadzu SPM-9600 microscope and the vibration isolation table.

## 2.4 X-ray diffraction

X-ray diffraction is widely used as a method to determine non-destructively thin lattice parameters, film orientation, and crystallinity. Because the wavelength of x-rays is close to the order of magnitude of the lattice constant of typical crystals, x-rays incident on a sample crystal are scattered by the electrons contained in each atom. An X-ray diffraction pattern can be measured by measuring the angular distribution of scattered

X-rays as a function of the incident x-ray angle relative to the crystal axes. The condition under which the x-rays are scattered by atoms is given by Bragg's formula

$$2d_{hkl} \sin \theta = n\lambda, \quad (2.1)$$

where  $\lambda$  is the wavelength of the incident X-rays,  $d$  is the lattice parameter,  $\theta$  is the diffraction angle, and  $n$  is a positive integer. Since the materials studied here are cubic, grown on isostructural substrates, it is sufficient to perform symmetric  $\theta - 2\theta$  diffraction scans that measure the out-of-plane lattice parameter by recording the  $\theta$  angle of (usually) the (002) diffraction peak.

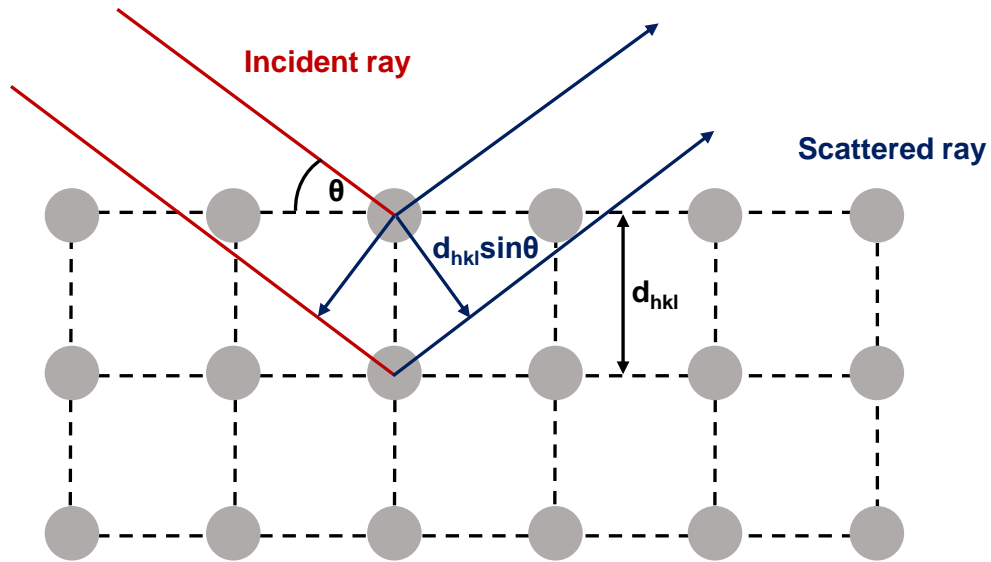


Figure 2.8: illustration of Bragg's condition in symmetric out-of-plane x-ray diffraction measurement.

Figure 2.9 shows the positional relationship between the x-ray source, the detector, and the sample in a actual measurement. The angle formed by the sample and the X-ray is defined as  $\omega$ . For thin film analysis, only two scan types were used,  $\omega - 2\theta$  scans to measure the lattice constants and  $\omega$  scans (rocking curve scan) to measure crystallinity. Symmetric  $\omega = \theta$  scans ( $\theta - 2\theta$ ) measure radial sections of the reciprocal lattice space (Fig. 2.10(a)), while  $\omega$  scan correspond to circular cuts (Fig. 2.10(b)).



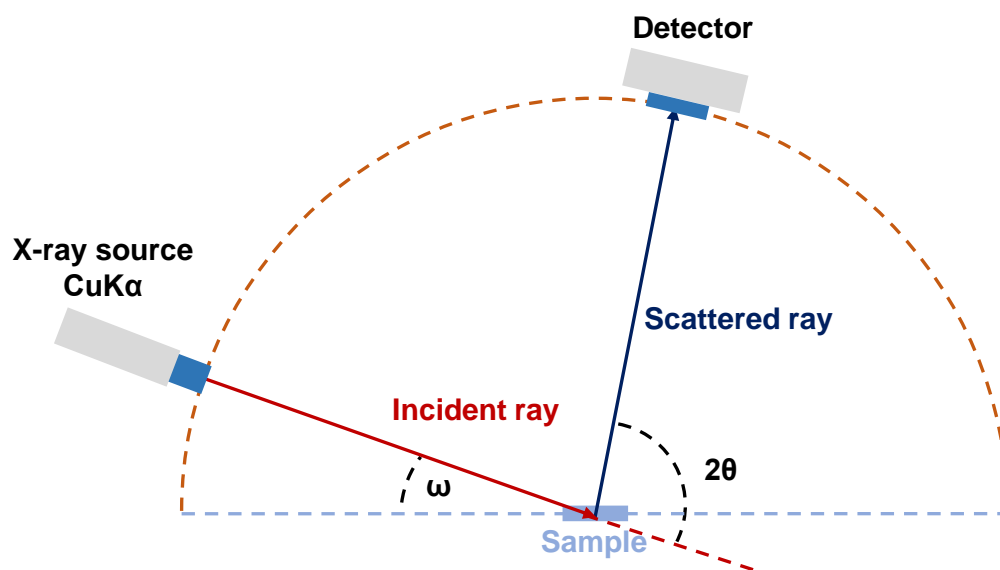


Figure 2.9: Schematic illustration of the geometry.

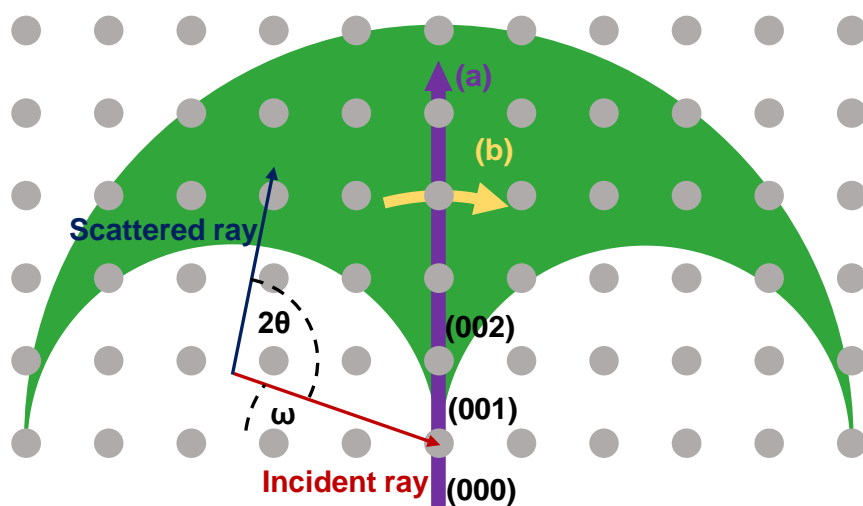


Figure 2.10: Schematic illustration of the various x-ray scans in the reciprocal space.

An X'Pert-MRD (Philips) diffractometer was used to obtain the diffraction patterns. In this machine, CuK $\alpha$  radiation was used. The CuK $\alpha$  line contains two close wave-

lengths,  $\text{CuK}\alpha_1(\lambda = 1.5405929(5)\text{\AA})$  and  $\text{CuK}\alpha_2(\lambda = 1.54444274(5)\text{\AA})$ . Strong and sharp diffraction peaks may thus show a split structure. The splitting can be eliminated by using a Ge crystal monochromator filter in the beam path, but at a cost of longer measurement time due to reduced x-ray intensity.

## 2.5 Optical absorbance measurement

Transmittance of the thin films was measured with a UV-Vis-NIR spectrometer. Special substrates with polished back surfaces were used for optical measurements to reduce scattering of incident light. All thin films for light transmittance measurements were grown on double sided polished  $\text{SrTiO}_3$  substrates. The spectra were collected with a Jasco V-570 UV-Vis-NIR spectrometer. The Spectrometer can measure the transmittance by calculating the ratio of the intensity of monochromatic transmitted and incident light,

$$T = \frac{I}{I_0}, \quad (2.2)$$

where  $I_0$  is the intensity of the incident light,  $I$  is the intensity of the transmitted light, and  $T$  is the calculated transmittance. Absorbance and absorption coefficient are calculated from the Lambert-Beer law

$$A = -\log \frac{I}{I_0} = -\log T, \quad (2.3)$$

$$\alpha = -\frac{1}{l} \ln\left(\frac{I}{I_0}\right) = -\frac{1}{l} \ln T, \quad (2.4)$$

where  $A$  is the absorbance,  $l$  is the film thickness and  $\alpha$  is the absorption coefficient ( $\text{cm}^{-1}$ ). By comparing the results of UV-Vis-NIR spectroscopy and X-ray photoelectron spectroscopy, it is possible to estimate the valence of dopants in  $\text{SrTiO}_3$  films. For example, for  $\text{Rh}^{4+}$  in  $\text{Rh}:\text{SrTiO}_3$ , the absorption peak derived from the acceptor level of  $\text{Rh}^{4+}$  is observed at around 580 nm. The valence of Rh was determined by the presence of that peak.

## 2.6 X-ray photoelectron spectroscopy

X-ray photoelectron spectroscopy is widely used as a method for identifying elements and valence states in materials. In this study, it was used as a way to determine the valence of Rh dopants. When monochromatic x-rays irradiate a material, photoelectrons are emitted by the photoelectric effect (Fig.2.11). The valence state of the

dopant can be determined by measuring the binding energy of a dopant core level. When monochromatic X-rays are used as a light source, this method is called X-ray photoelectron spectroscopy. The kinetic energy of the photoelectron emitted by X-ray photoelectron spectroscopy is given by the following equation

$$E_{kin} = h\nu - E_{binding} - \Phi, \quad (2.5)$$

where  $E_{kin}$  is the kinetic energy of the emitted photoelectrons,  $h\nu$  is the energy of the incident X-rays,  $\Phi$  is the work function of the sample, and  $E_{binding}$  is the energy of the electrons inside the sample occupying a particular energy level. Since  $h\nu$  and  $\Phi$  are known values,  $E_{binding}$  can be calculated by measuring  $E_{kin}$ . The emitted electrons have information on the core level and the valence band of the substance. With this information, it is possible to know which elements are present in a sample and to determine the chemical bonding state. In general, the binding energy increases for higher valence states.

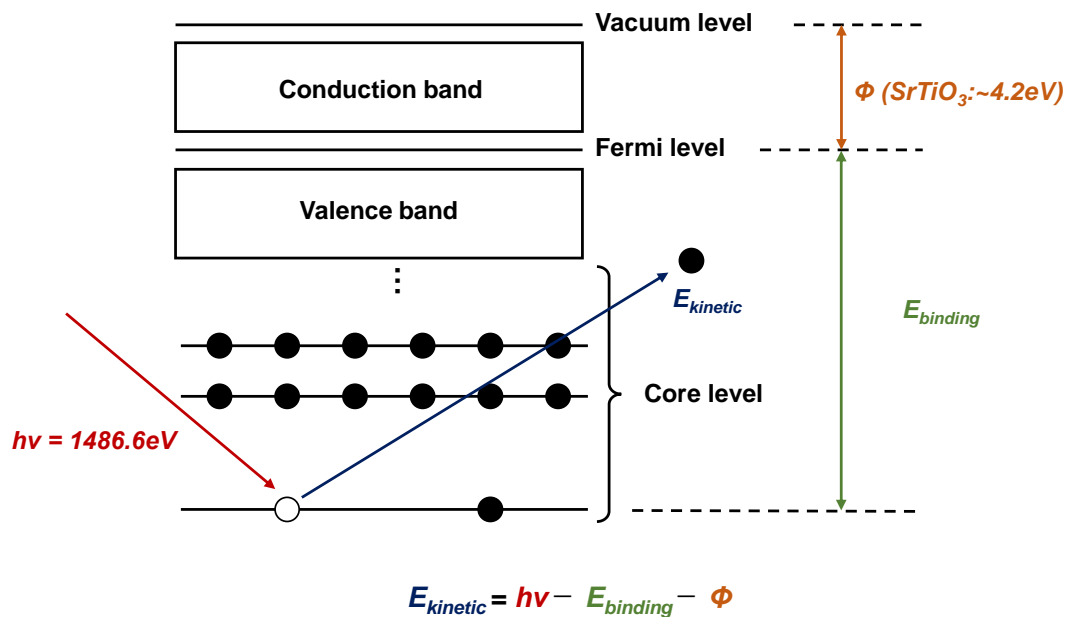


Figure 2.11: Principle of XPS.

Photoelectrons can only be emitted from a thin surface layer of a material. It is thus very important to know how deep the probing of the electronic information by XPS can

be, because there is a possibility that the chemical composition or the electronic state is different from bulk close to surface due to adsorbed contaminants or reactions with the atmosphere. Most of the electrons generated by the incident X-rays are absorbed in the material without emission. Only a small amount of photoelectron close to the surface can escape into vacuum and reach the detector. The probing depth of XPS is given by the inelastic mean free path of electrons. In this study, IMFP was approximated by using the plot in Figure 2.12. Since electrons are constantly emitted during measurement, and insulating sample would become positively charged, whereby the kinetic photoelectron energy emitted is shifted. In order to avoid this, all thin films were grown on conducting Nb0.05wt%:SrTiO<sub>3</sub> substrates.

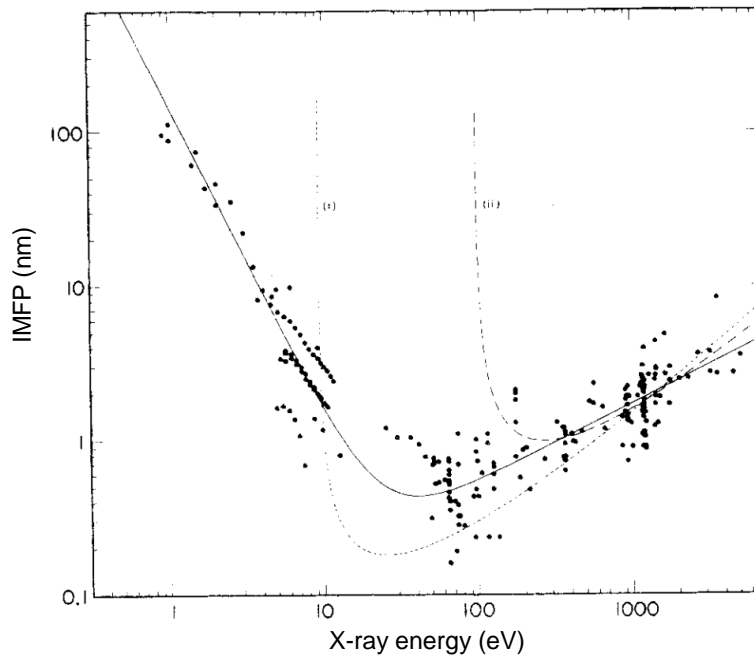


Figure 2.12: Inelastic mean free path of electrons vs x-ray energy [16].

## 2.7 Photoelectrochemical measurement

The photoelectrochemical activity of the thin film samples was evaluated by cyclic voltammetry measurements. In cyclic voltammetry, the potential of the working electrode is cycled repeatedly between a minimum and a maximum value relative to a reference electrode. The cycling is usually done in slow linear bias sweeps while

the current between the working and counter electrodes is measured. For the water splitting reaction, the measured current is proportional to the number of hydrogen molecules released at the photocathode surface if no sacrificial reactions occur on the photoelectrode surface. Light can be illuminated on the sample surface during the voltammetry measurement. A convenient technique is to chop the incident light at approximately 1 second intervals, allowing the photocurrent to be separated from a dark-condition leak current. Additionally, the incident light chopping is useful for estimating the role of trapping in the photoelectrode, which can be seen in the form of sharp current transients at the start of each light illumination pulse.

Figure 2.13 shows a schematic diagram of a sample mounted on a support for photoelectrochemical measurement. A  $\text{Sr}_2\text{RuO}_4$  thin film was used as a metallic bottom electrode for the thin film samples.  $\text{Sr}_2\text{RuO}_4$  can grow epitaxially on the  $\text{SrTiO}_3$  substrate and forms an Ohmic junction with the doped  $\text{SrTiO}_3$  thin film. A lead wire was attached to the edge of the thin film sample and the  $\text{Sr}_2\text{RuO}_4$  layer with a droplet of liquid InGa alloy.

The electrochemical cell (Fig. 2.14) is made of polytetrafluoroethylene, which is stable in acidic and alkaline solutions. The aqueous electrolyte solution was bubbled with pure nitrogen gas for at least 30 minutes to remove dissolved oxygen before the electrolyte was allowed to flow into the electrochemical cell.

While sweeping the applied bias, the photocurrent was measured under chopped light illumination (Fig. 2.15) with a potentiostat (Bio-Logic SP-150). Pt wire was used as the counter electrode in the cell and the applied bias was referenced to Ag/AgCl sat. KCl (eDAQ; ET072) reference electrode.

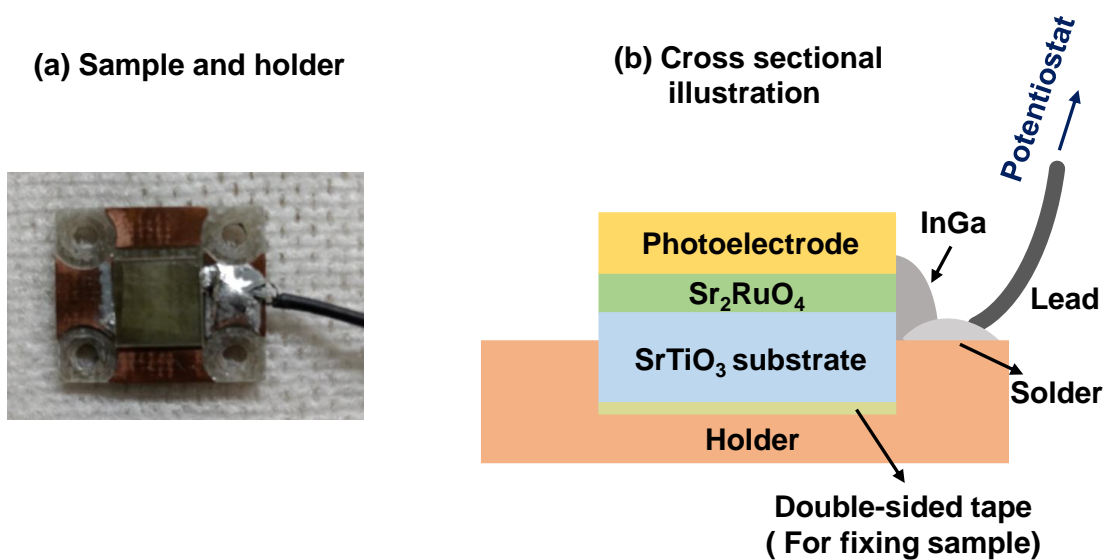


Figure 2.13: (a) Schematic diagram of a sample and holder. (b) Cross-sectional illustration of sample and electrical connections.

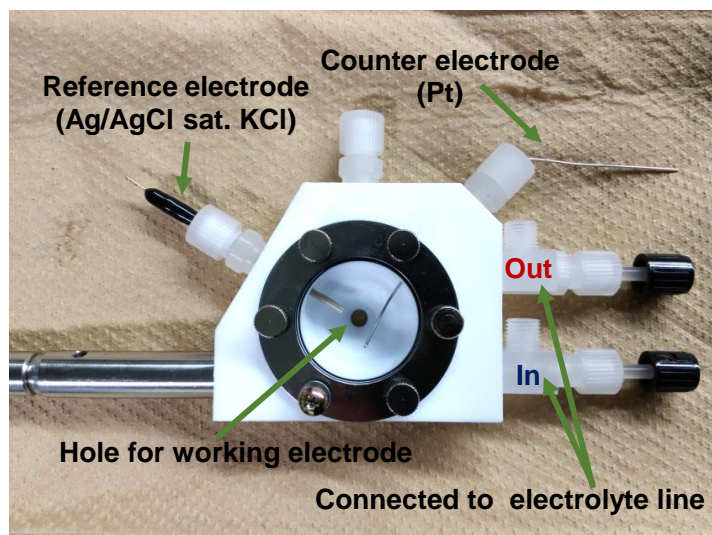


Figure 2.14: A view of the photoelectrochemical cell made of polytetrafluoroethylene.

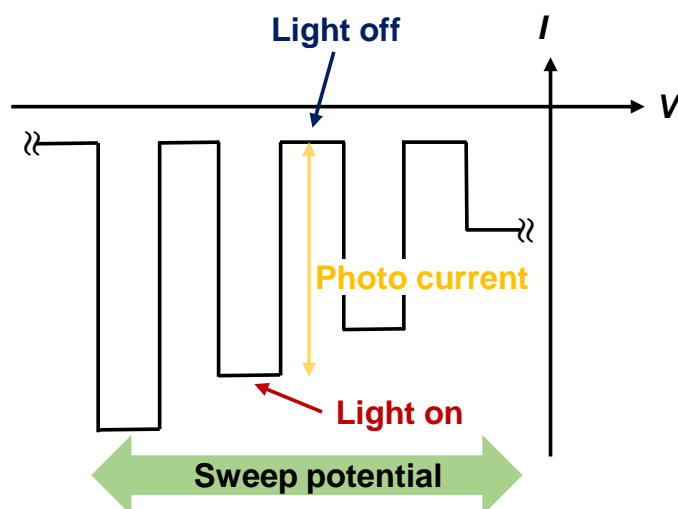


Figure 2.15: Chopped light voltammetry measurement. When light is off, the potentiostat measures the dark (background) current. When the light is on, the voltammogram shows the contribution of the photoinduced current that is proportional to the amount of evolved hydrogen gas in a cathodic water splitting reaction.

Cyclic voltammetry was measured under white light and monochromatic light. An Asahi Spectra LAX101 Xenon lamp was used as a light source of white light, and a tunable BML-10J Xe light source was used for monochromatic measurements. The average optical power density of the irradiated monochromatic light was measured with a ThorLabs PM100D power meter. It is possible to calculate the quantum efficiency of the photoelectrode from the photocurrent measured under monochromatic light and the intensity of light irradiated on the photoelectrode. The incident photon to current efficiency (IPCE) and absorbed photon to current efficiency (APCE) were calculated by

the following formulae

$$\begin{aligned}
 IPCE(\%) &= \frac{\text{Number of photocarriers used for electrochemical reaction}(1/cm^2)}{\text{Incident photon flux}(1/cm^2)} \times 100(\%) \\
 &= \frac{hc}{e} \frac{\text{Photocurrent density}(mA/cm^2)}{\text{wavelength}(nm) \times \text{Light Itensity}(mW/cm^2)} \quad (2.6)
 \end{aligned}$$

$$\begin{aligned}
 APCE(\%) &= \frac{\text{Number of photocarriers used for electrochemical reaction}(1/cm^2)}{\text{Absorbe photon flux}(1/cm^2)} \times 100(\%) \\
 &= \frac{hc}{e} \frac{\text{Photocurrent density}(mA/cm^2)}{\text{wavelength}(nm) \times \text{Light Itensity}(mW/cm^2) \times (1 - e^{-\alpha d})} \quad (2.7)
 \end{aligned}$$

where  $h$ ,  $c$ , and  $e$  are the Planck constant, speed of light, and elementary charge, respectively.  $\alpha$  is the absorption coefficient, and  $d$  is the film thickness of the photoelectrode.



## Chapter 3

# Avoiding Rh clustering

### 3.1 Optimizing Rh<sup>3+</sup>:SrTiO<sub>3</sub> growth

The formation of defect clusters in Rh:SrTiO<sub>3</sub> can be identified as one of the main causes for the unexpectedly low energy conversion efficiency. There are three main types of defects that appear to occur in Rh<sup>3+</sup>:SrTiO<sub>3</sub> thin films grown at low oxygen pressures. The most common defect type is the oxygen vacancy cluster, which is a common feature for reduced SrTiO<sub>3</sub> and is known to produce in gap states. The Rh-related defect clusters are Rh pairs, where an oxygen vacancy stabilizes the Rh<sup>3+</sup> state in two neighboring Rh atoms. The third defect is the formation of metallic Rh clusters and possible segregation of macroscopic metal nanostructures in the SrTiO<sub>3</sub> host lattice. It is thus important to consider thin film growth methods that may reduce the number of defects in Rh:SrTiO<sub>3</sub> films.

In order to reduce Rh clustering, the Rh<sup>3+</sup>:SrTiO<sub>3</sub> film growth conditions were optimized by adjusting the ablation laser fluence. The main effect of this optimization is to try to tune the cation Sr:(Ti,Rh) stoichiometry to as close as possible of the ideal ratio of 1:1. A series of Rh<sup>3+</sup>:SrTiO<sub>3</sub> films were growth at 700°C and an oxygen pressure of 10<sup>-6</sup> Torr. These conditions are similar to those that have been used in earlier studies, [8] except for the systematic tuning of the laser fluence. All films were grown on single-side-polished SrTiO<sub>3</sub> substrates. The XRD 2 $\theta$ / $\theta$  scans for this sample series are shown in Fig. 3.1. As shown by the narrow scans in the vicinity of the perovskite (002) peak, the Rh<sup>3+</sup>:SrTiO<sub>3</sub> film peaks were always split from substrate peak. Since these are essentially homoepitaxial films with a relatively low doping level of just a few percent, the film peaks should overlap with the substrate peaks. The XRD data shows that the film lattice expansion, which is proportional to the diffraction peak shift, increases with

increasing laser fluence. From these result, it appears that a fluence of  $\sim 0.31 \text{ J/cm}^2$  is the optimal laser energy density for  $\text{Rh}^{3+}:\text{SrTiO}_3$  growth. Further fluence reduction is impossible due to an ablation threshold which is close to this value. However, even at optimum laser fluence, a slight lattice expansion of  $\sim 0.008 \text{ \AA}$  was observed. It thus appears that even at close to optimal stoichiometry, the film still contains lattice defects despite the cation stoichiometry adjustments.

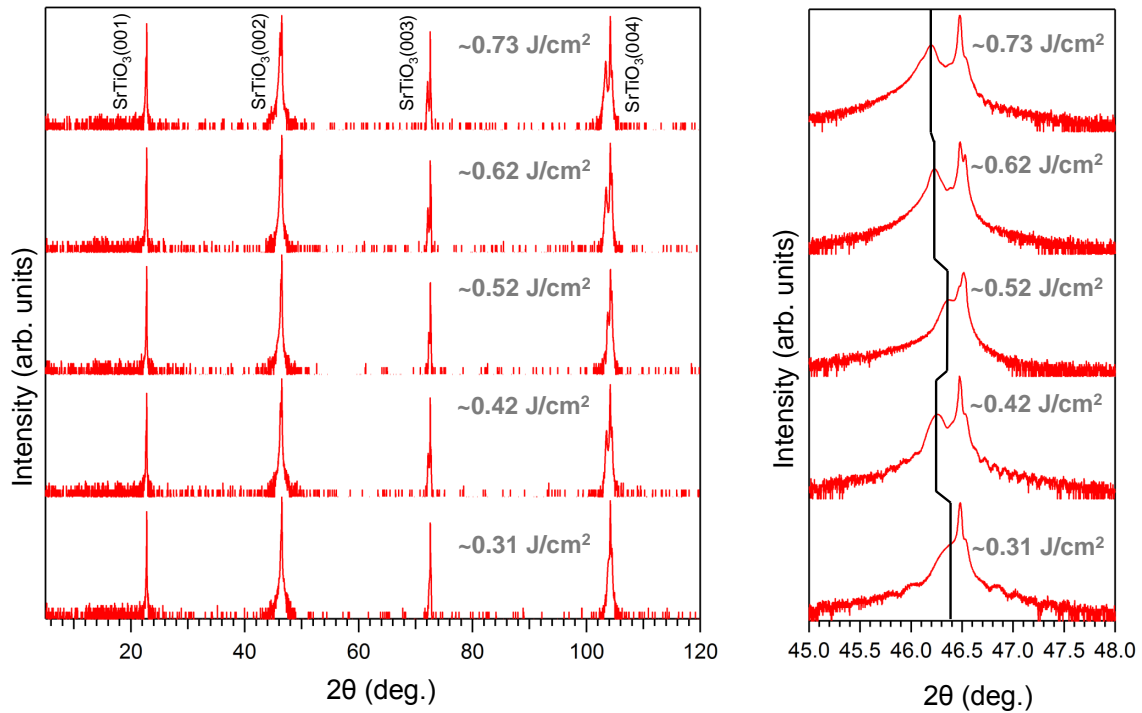


Figure 3.1: XRD  $2\theta/\theta$  scans of  $\text{Rh}^{3+}:\text{SrTiO}_3$  films grown at various laser fluences. A  $\text{SrTiO}_3$  substrate was used. The film thickness was between 60 and 100 nm. Wide range scan show no secondary phases or orientations. The narrow scans indicate that the lattice parameter of the film is larger than the substrate for all laser fluence values.

### 3.2 Robust Rh valence in $\text{Rh}^{3+}:\text{SrTiO}_3$

The easiest way to determine the average Rh valence in a film sample is to look at the optical absorption spectrum, as has been shown in earlier studies on  $\text{Rh}:\text{SrTiO}_3$ . [8]. The most significant difference in the absorption spectra is the appearance of a broad

absorption feature centered at around 560 nm for  $\text{Rh}^{4+}:\text{SrTiO}_3$ . This feature has been assigned to an excitation from the valence band to the unoccupied  $\text{Rh}^{4+}$  midgap level [17]. If a film has no defects the Rh valence should depend on the average oxygen stoichiometry. A film grown at a low oxygen pressure has a high density of oxygen vacancies, which reduce the Rh dopants to a 3+ state. Oxygen or air annealing should gradually reduce the oxygen vacancy density and thus convert the Rh dopants to the 4+ state. This change should be detectable in the absorption spectra as an increase of absorption at around 560 nm and the film color should change from yellow to purple.

This experiment was carried out for the  $\text{Rh}^{3+}:\text{SrTiO}_3$  films grown at optimal conditions with the best achievable cation stoichiometry. For this measurement, 400 nm thick films were grown on double-side-polished  $\text{SrTiO}_3$  substrates. The result is shown in Fig. 3.2. As expected, absorption did increase at 560 nm, indicating that Rh valence change did occur. However, the absorption spectrum change is much smaller than expected. When observed by eye, as shown in the photographs in Fig. 3.3, the original yellow film color is nearly unchanged after air annealing. Comparing the two images, it appears that only one part of the film, in the upper left part of the substrate, slightly changed color. Most of the film, however, was still dark yellow after air annealing. This result confirms the XRD result, which indicated that defects are still present in films grown at reducing conditions. The lack of reversible Rh valence suggests that the defects are related to dopant clustering rather than the  $\text{SrTiO}_3$  host lattice.

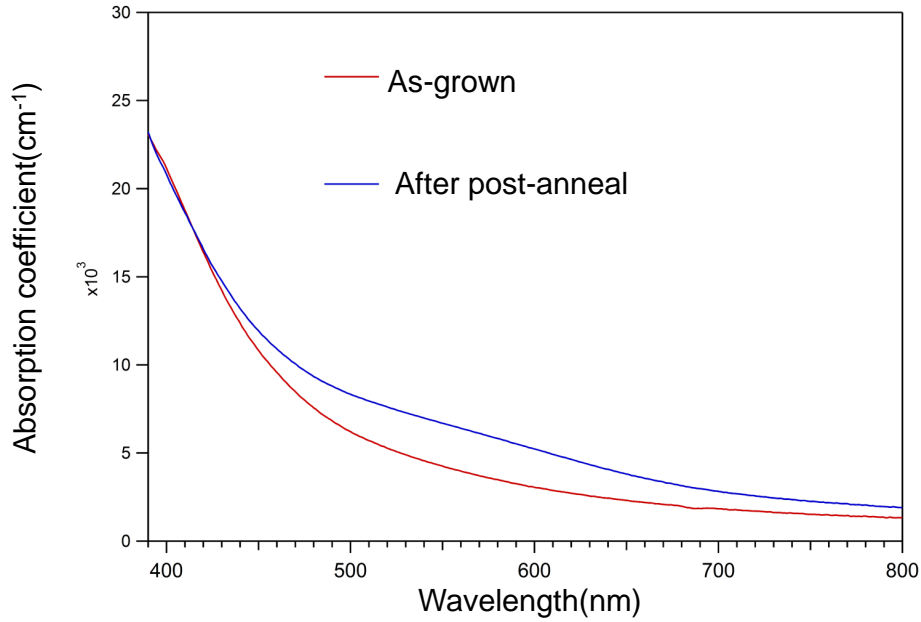


Figure 3.2: Absorption spectra of a Rh:SrTiO<sub>3</sub> film after growth at 10<sup>-6</sup> Torr and after post-annealing in air. The increase of absorption at around 560 nm indicates a partial conversion of Rh<sup>3+</sup> to Rh<sup>4+</sup>.

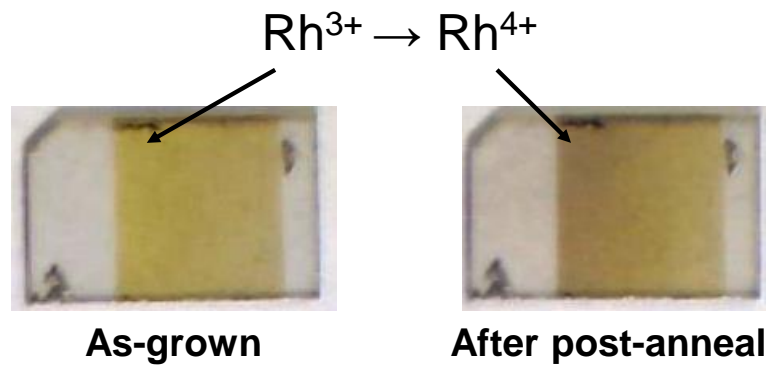


Figure 3.3: Pictures of a Rh:SrTiO<sub>3</sub> film sample grown at 10<sup>-6</sup> Torr. The yellow color corresponds to the Rh<sup>3+</sup> dopant state. Pictures show the sample after growth (left) and after post-annealing in air (right).

The stoichiometry tuning experiments showed that the dopant clustering is not

purely caused by strontium vacancies or other stoichiometry errors in the  $\text{SrTiO}_3$  lattice. Another possibility is that dopant clustering occurs due to the presence of oxygen vacancies when a film is grown at reducing conditions. This may promote the formation of Rh metal clusters or clusters that combine Rh dopants with oxygen vacancies.

A different way of obtaining a  $\text{Rh}^{3+}:\text{SrTiO}_3$  film was thus tested. A  $\text{Rh}^{4+}:\text{SrTiO}_3$  can be grown in oxidizing conditions, which reduces the number of oxygen vacancy defects in the crystal during film growth. This may lead to full oxidation of Rh and uniform doping of Rh at the Ti site without cluster formation. This approach has already been tried in a previous study [8]. It should then be possible to obtain a  $\text{Rh}^{3+}:\text{SrTiO}_3$  film by vacuum annealing a fully oxidized, defect-free film. However, in an earlier study, the  $\text{Rh}^{4+}$  reduction to  $\text{Rh}^{3+}$  was incomplete after vacuum annealing. XPS analysis showed the presence of both of  $\text{Rh}^{4+}$  and  $\text{Rh}^{3+}$  components.

There are several possibilities why vacuum reduction was not successful in the earlier study. The first possibility is that the annealing was not sufficiently reducing, either because the temperature was too low or the oxygen background pressure was too high. The annealing conditions in the previous study were  $10^{-6}$  Torr,  $700^\circ\text{C}$ , which is the same as the  $\text{Rh}^{3+}:\text{SrTiO}_3$  growth conditions, but it may be insufficient for introducing oxygen vacancies into the bulk of film after growth. This may lead to only partial conversion of  $\text{Rh}^{4+}$  to  $\text{Rh}^{3+}$ , even in the surface layer of the film that is probed by XPS.

The second possibility is that even in a  $\text{Rh}^{4+}$  film, metal clustering is still present. The presence of metallic Rh has not been observed in  $\text{Rh}:\text{SrTiO}_3$  films grown in oxidizing conditions, but this does not rule out the presence of cluster defects in the bulk of the film that cannot be probed by XPS.

Finally, the reduction process may have failed due to cation stoichiometry problems, since the samples used in earlier work were not specifically optimized in this regard.

### 3.3 Optimizing $\text{Rh}^{4+}:\text{SrTiO}_3$ stoichiometry

The exact stoichiometry of a complex oxide film grown by PLD may change slightly when the background oxygen pressure is changed. This stoichiometry change is related to change in the shape and size of the plasma plume formed during ablation and the gas-phase reactions that occur in the vacuum chamber. At  $10^{-6}$  Torr, as used for the growth of  $\text{Rh}^{3+}:\text{SrTiO}_3$  films, the PLD process works in a molecular beam regime, where few collisions occur between the ablated atoms and ambient oxygen. At 100 mTorr, which is needed to grow a fully oxidized film, the PLD plasma plume has many collisions

with the ambient oxygen gas. The film stoichiometry thus has to be re-optimized for different growth pressures. Since this re-optimization was not done in earlier work, it is possible that the lack of  $\text{Rh}^{4+}$  conversion to  $\text{Rh}^{3+}$  upon vacuum annealing was caused by additional crystal defects related to stoichiometry errors.

$\text{Rh}^{4+}:\text{SrTiO}_3$  film stoichiometry was therefore optimized in this work by adjusting the ablation laser fluence and observing the lattice parameter expansion of the films. Based on earlier work, it was known that fully oxidized  $\text{Rh}^{4+}:\text{SrTiO}_3$  films can be grown at  $700^\circ\text{C}$  and an oxygen pressure of  $10^{-1}$  Torr. [8]. The XRD  $2\theta/\theta$  scans of  $\text{Rh}:\text{SrTiO}_3$  films grown at these conditions but at different laser fluences are shown in Fig. 3.4. As shown by the narrow scans close to the (002) perovskite diffraction peak, splitting is still seen for several samples, indicating that the film lattice parameter is slightly larger than the  $\text{SrTiO}_3$  substrate. However, the lattice expansion was almost zero for fluence values of  $0.5 \text{ J/cm}^2$  or higher. Lower ablation laser fluence caused a systematic lattice parameter expansion.

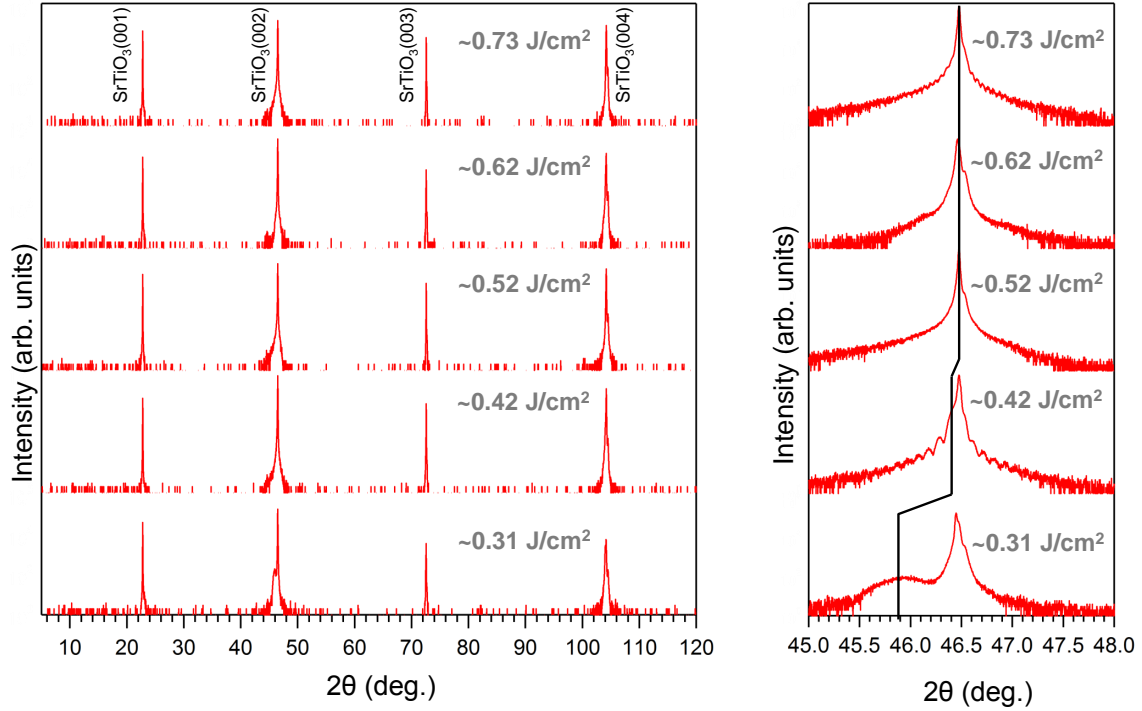


Figure 3.4: XRD  $2\theta/\theta$  scans of  $\text{Rh}^{4+}:\text{SrTiO}_3$  films grown at various laser fluences on  $\text{SrTiO}_3$  substrates at an oxygen pressure of 100 mTorr. The film thickness was between 80 and 120 nm. Wide range scans show no misoriented phases. Narrow scans of the (002) peak show that lattice expansion only occurs at low laser fluence, below  $0.5 \text{ J/cm}^2$ .

### 3.4 Reversible Rh valence

A fully oxidized  $\text{Rh}^{4+}:\text{SrTiO}_3$  film with optimal stoichiometry was grown at a fluence of  $0.62 \text{ J/cm}^2$  on a double-side-polished  $\text{SrTiO}_3$  substrate. The film thickness was 400 nm. The absorption spectrum of the as-grown film shown in Fig. 3.5 and a picture of the sample can be seen in Fig. 3.6. The 560 nm absorption band can be clearly seen in the spectrum and the film color is purple, as expected for a fully oxidized film with a pure  $\text{Rh}^{4+}$  dopant state. This film was reduced by annealing at an oxygen pressure of  $10^{-6}$  Torr and  $800^\circ\text{C}$  for 3 hours. The absorption spectrum change can be seen in Fig. 3.5. It is clear that the absorption peak at around 560 nm disappeared completely and the color of the film changed from purple to yellow, as can be seen in Fig. 3.6(b).

This indicates that the Rh dopant valence was successfully reduced from  $\text{Rh}^{4+}$  to  $\text{Rh}^{3+}$ .

The film sample was subsequently re-oxidized by post-annealing in air and both the absorption spectrum, Fig. 3.5(c), and the film color, Fig. 3.6(c), recovered. The 560 nm absorption feature amplitude is similar to the original film and the color returned to purple. This behavior is in stark contrast to the  $\text{Rh}^{3+}:\text{SrTiO}_3$  film that was originally grown at reducing conditions ( $10^{-6}$  Torr oxygen pressure), for which Rh valence reversal was not possible by annealing.

This series of experiments shows that growing a Rh:doped  $\text{SrTiO}_3$  film at reducing conditions generates dopant cluster defects that essentially lock the valence state to  $\text{Rh}^{3+}$ . The most likely cause for this is the formation of dopant clusters with oxygen vacancies. Since cation diffusion does not occur in a perovskite lattice at the typical annealing temperatures of  $700^\circ\text{C}$  or lower, these clusters cannot be eliminated in post-deposition heat treatments. To fabricate cluster-free Rh-doped films, it is necessary to grow a fully oxidized film where  $\text{Rh}^{4+}$  ions substitute at the  $\text{Ti}^{4+}$  site and to carefully optimize the perovskite cation stoichiometry. Under these conditions, it is possible to obtain a film with a reversible dopant valence. The main merit of such a film is a significantly reduced density of defects that may work as photocarrier trap and recombination centers.



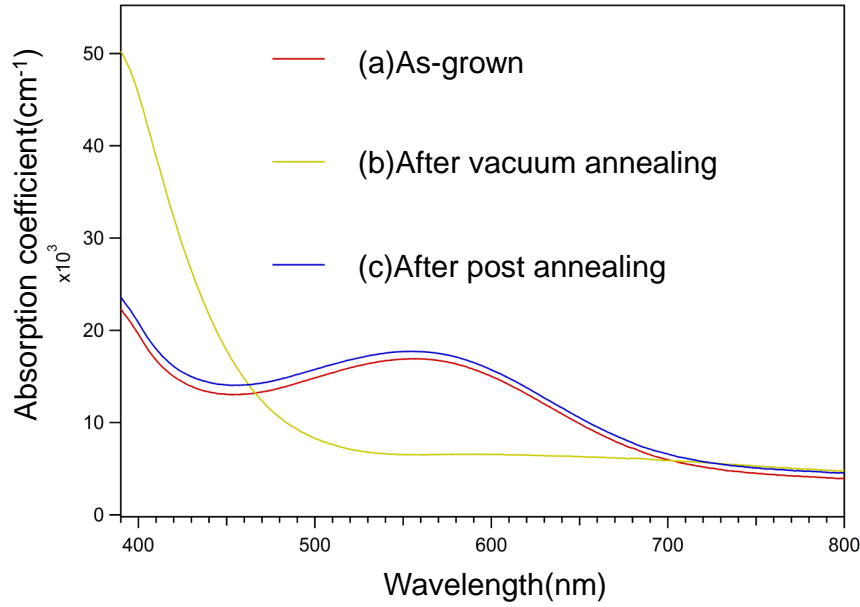


Figure 3.5: Absorption spectra of (a) Rh:SrTiO<sub>3</sub> film grown at 10<sup>-1</sup> Torr. The absorption peak at 560 nm indicates that the film is fully oxidized and Rh is in the 4+ state. (b) The same film, after being reduced by vacuum annealing at 800°C, 10<sup>-6</sup>Torr for 3 hours. The spectrum corresponds to a pure Rh<sup>3+</sup> state. (c) Film (b) post-annealed at 400°C in air for 6 hours. The film is re-oxidized and the absorption spectrum recovers the original shape. The Rh dopant valence has thus been converted back to the 4+ state.

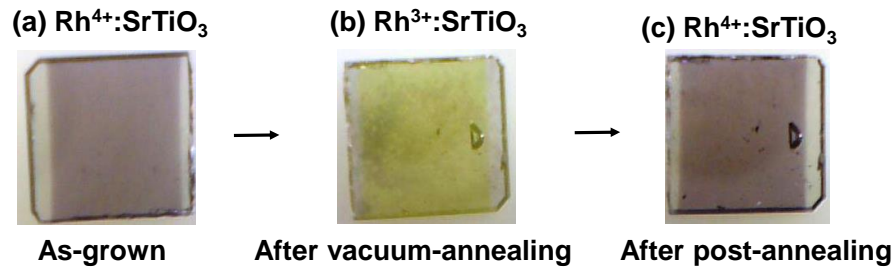


Figure 3.6: Pictures of the reversible valence film sample. (a) As-grown, purple, Rh<sup>4+</sup>, (b) after vacuum annealing, yellow, Rh<sup>3+</sup>, (c) after post annealing in air, purple, Rh<sup>4+</sup>.

In addition to the reversible Rh valence state, the absorption coefficient of the

$\text{Rh}^{3+}:\text{SrTiO}_3$  film produced by vacuum annealing an optimized  $\text{Rh}^{4+}:\text{SrTiO}_3$  film was two times higher than that of a  $\text{Rh}^{3+}:\text{SrTiO}_3$  that was directly grown at  $10^{-6}$  Torr. One should consider the possibility that a lot of Rh oxide species decomposed at  $10^{-6}$  Torr. There can be several reasons for the improved light absorption. The simplest reason is that the Rh concentration in the film is higher, although the same ablation target was used. The vapor pressure of various materials related to this film growth are shown in Fig. 3.7.  $\text{Rh}_2\text{O}_3$  is more volatile than others components, which means that when a  $\text{Rh}:\text{SrTiO}_3$  film is grown at low absolute pressure, Rh may have formed  $\text{Rh}_2\text{O}_3$  on the film surface and at  $10^{-6}$  and  $700^\circ$  the Rh oxide would evaporate. Depositing a film at a higher background pressure inhibits the evaporative loss of Rh and therefore films grown at 100 mTorr may retain more Rh.

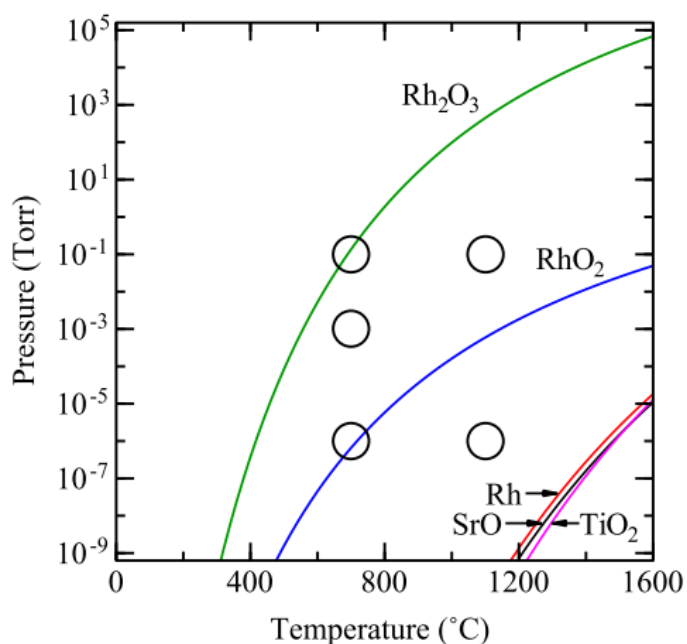


Figure 3.7: Vapor pressures of Rh metal, SrO,  $\text{TiO}_2$  and Rh oxide species. [8]

XPS was used to analyze the Rh valence in the optimized  $\text{Rh}:\text{SrTiO}_3$  thin films. For this experiment,  $\text{Rh}:\text{SrTiO}_3$  films were grown on conducting  $\text{Nb}(0.05\text{w}\%):\text{SrTiO}_3$  substrates at the optimum growth conditions as discussed earlier. the film thickness of these samples was about 20 nm. The energy of monochromatic x-ray was 1486.6 eV. For this excitation energy, the probing depth of XPS is  $\sim 3$  nm. the Rh valence state was determined by looking at the binding energy shift of the Rh  $3d_{5/2}$  core-level peak.

The binding energies assume a surface work function of 4.2 eV. The core level peak positions were referenced to Ti and O core level peak positions. The Rh core level positions were taken from literature references for various Rh oxides [18–20]. The XPS core level profiles are shown in Fig. 3.8. All films exhibited an almost pure  $\text{Rh}^{4+}$  state with no observable  $\text{Rh}^{3+}$  component.

The XPS analysis indicates that even when the film color is yellow, which means that the Rh dopant is in the desired  $\text{Rh}^{3+}$  state in the bulk of the film, the easy reversibility of the dopant valence by oxidation or reduction leads to rapid oxidation of the surface when exposed to air, even at ambient conditions. While this is an indication of the high crystalline quality of the samples, it also suggests that oxygen vacancy control of the Rh valence is fundamentally flawed, because the dopant valence state cannot be fixed at the desired 3+ value. Instead, the surface valence can change by exposure to air and is likely to change when the film is used as a photoelectrode in an electrochemical cell. A different route to stabilizing the  $\text{Rh}^{3+}$  state must thus be found.

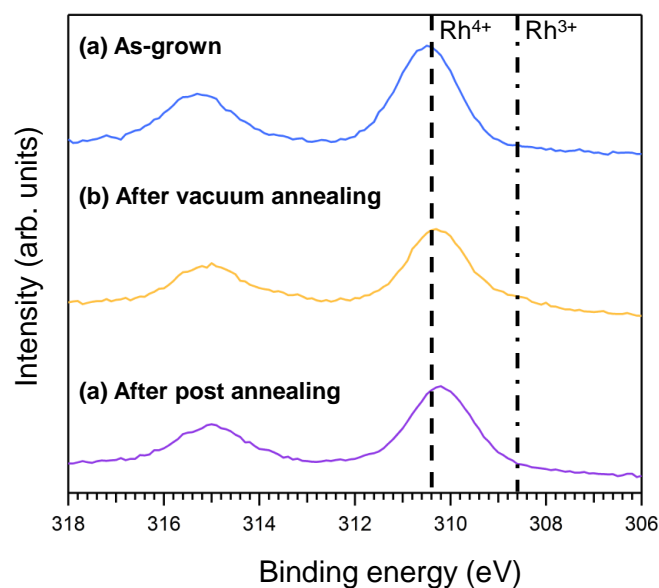


Figure 3.8: X-ray photoelectron spectra. (a) A film grown at 700°C,  $10^{-1}$  Torr. (b) Film (a) annealed at 800°C,  $10^{-6}$  Torr for 3 hours. (c) Film (b) annealed re-oxidized by annealing in air. The binding energies were calibrated against the Ti  $2p_{3/2}$  core level peak position at 559.1 eV [22].

# Chapter 4

## Rh valence control by La co-doping

### 4.1 Introduction

Attempts to control the Rh dopant valence in  $\text{SrTiO}_{3-\delta}$  by changing the oxygen vacancy density  $\delta$  was ultimately successful, but at the same time showed that the vacancy density can change easily, even in ambient atmospheric conditions. This means that Rh valence control by oxygen vacancies cannot be used in practical photoelectrochemical electrode materials.

Despite this negative conclusion, the experiments described in the previous also suggest a possible solution. It was found that if dopant clusters form in  $\text{SrTiO}_3$ , these clusters are surprisingly robust. In particular,  $\text{Rh}^{3+}:\text{SrTiO}_3$  films grown at low pressure could not be fully oxidized due to the stability of Rh clusters. The same idea can thus be used to obtain a material where the rh valence is fixed at the 3+ state, but without using the volatile oxygen vacancies as a source of the necessary electrons. Instead, it is possible to dope La at the Sr site in  $\text{SrTiO}_3$ . Since La valence is 3+ while the Sr valence is 2+, such doping produces free carriers. Indeed,  $\text{La}:\text{SrTiO}_3$  is a well-known metallic material. If, however,  $\text{SrTiO}_3$  is co-doped with both La and Rh in equal amounts, it should be possible to transfer one electron from La to Rh and thus stabilize the  $\text{Rh}^{3+}$  state without creating additional free carriers. This would maintain the *p*-type character of  $\text{Rh}:\text{SrTiO}_3$ , which is needed for a hydrogen evolution photoelectrode material.

Another problem solved by (La,Rh) co-doping is the elimination of oxygen vacancies. Oxygen vacancies in  $\text{SrTiO}_3$  are known to cluster and such vacancy clusters form in-gap states close to the bottom of the conduction band. For a photoelectrode material, this is undesirable, because such shallow in-gap states function as photocarrier trap centers that lead to a decrease of carrier mobility and photoelectrochemical activity. In

particular, carriers from deeper parts of the photoelectrode cannot reach the electrode surface before being trapped and recombined.

There are numerous co-doped photocatalyst studies, for example (Sb,Rh) [27,29,29], (Ta,Cr) [23,24], (Sb,Cr) [31](Cr,La) [30], (La,N) [26], (La,Rh) [32] co-doped SrTiO<sub>3</sub> and (Ta,Ni) [23], (Sb,Cr) [24], and (Sb,Rh) [25] co-doped TiO<sub>2</sub>. In particular, using La<sup>3+</sup> as a co-dopant is a promising route for enhancing photoelectrochemical activity of Rh:SrTiO<sub>3</sub>. The co-doping has been studied for bulk powder (La,Rh):SrTiO<sub>3</sub> photocatalysts and higher photocatalytic activity than Rh:SrTiO<sub>3</sub> has been observed. [32]

## 4.2 Preparing a (La,Rh):SrTiO<sub>3</sub> ablation target

The (La,Rh):SrTiO<sub>3</sub> powder was synthesized following the process used in previous studies. [8, 32] The starting materials were SrCO<sub>3</sub> (Wako Pure Chemical), TiO<sub>2</sub> (Wako Pure Chemical) and La<sub>2</sub>O<sub>3</sub>(Waco Pure chemical), and RhO<sub>2</sub> (Wako Pure Chemical). The powders were mixed with a small amount of ethanol. The target composition was slightly A-site rich, i.e., the (La,Sr):(Ti,Rh) ratio was 1.07. The target composition was thus Sr<sub>1.02</sub>La<sub>0.05</sub>Ti<sub>0.95</sub>Rh<sub>0.05</sub>O<sub>3</sub>. After mixing the starting materials, the powders were pre-calcined in air at 900°C for 1 hour, followed by calcining in air at 1100°C for 10 hours in an alumina crucible. For PLD targets, the powders were formed into pellets by powder molding in a press at 20 MPa, followed by final calcining in air at 1200°C for 24 hours. As can be seen in Fig. 4.1, the final pellet color was dark brown not yellow, which means that co-doping does not yet occur in the solid state reaction of the source materials.

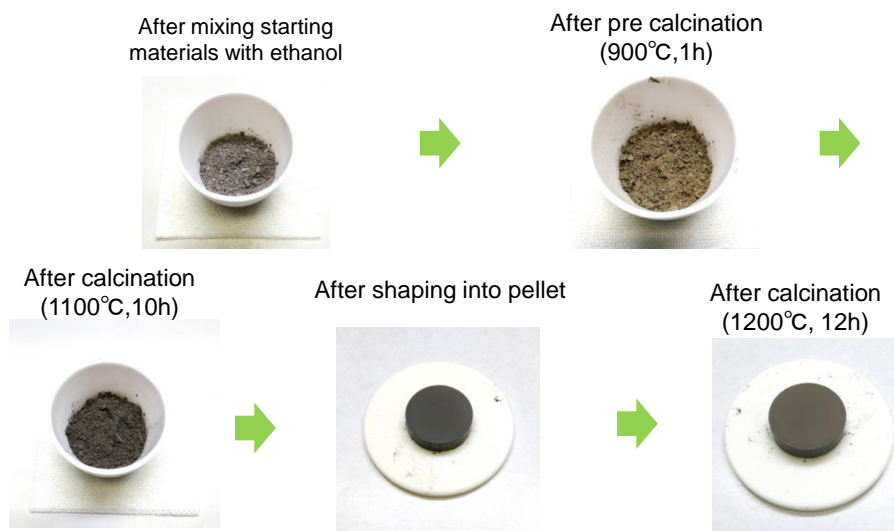


Figure 4.1: Target preparation process.

### 4.3 The effect of La,Rh co-doping on Rh valence

At first, the film growth conditions were examined. As was discussed in Chapter 3, Rh:SrTiO<sub>3</sub> film growth at low oxygen pressures, on the order of 10<sup>-6</sup> Torr is necessary for stabilizing the Rh<sup>3+</sup> state but also induces the formation of Rh clusters and possibly Rh clusters with oxygen vacancies. To avoid complications related to the presence of oxygen vacancies, it is thus better to grow the co-doped films at high pressures. Based on the results of Chapter 3.2, it is clear that Rh:SrTiO<sub>3</sub> does not form dopant clusters at 10<sup>-1</sup> Torr. therefore a growth temperature of 700°C and an oxygen pressure of 10<sup>-1</sup> Torr were selected as the film growth conditions for the (La,Rh):SrTiO<sub>3</sub> films.

The main purpose of co-doping with La in this film is to stabilize the Rh<sup>3+</sup> state. Therefore, a relatively thick, 400 nm film was grown on a double-side polished SrTiO<sub>3</sub> substrate at a laser fluence of 0.52 J/cm<sup>2</sup>. This laser fluence was found to be sufficient for obtaining close to ideal film stoichiometry at the 10<sup>-1</sup> Torr working pressure. The absorption spectrum of this film is shown in Fig. 4.2 and a picture of the sample can be seen in Fig. 4.3. For reference, the absorption spectrum of a Rh<sup>4+</sup>:SrTiO<sub>3</sub> thin film grown at 10<sup>-1</sup> Torr is also shown in Fig. 4.2. An increase in absorption near 560 nm that is characteristic of the Rh<sup>4+</sup> state was not observed in the as-grown (La,Rh):SrTiO<sub>3</sub> thin film. This is proof that the co-doping worked as designed and the Rh<sup>3+</sup> dopant

state could be stabilized in a film grown in oxidizing conditions. As shown by the comparison with the absorption spectrum of the  $\text{Rh}^{4+}:\text{SrTiO}_3$  film in Fig. 4.2, growing a film doped with Rh only will produce the  $\text{Rh}^{4+}$  state under the same growth conditions.

It is also necessary to verify that the Rh valence state is determined purely by the presence of La and is not affected by the oxygen balance. For this purpose, the co-doped film was additionally post-annealed in air to fill any remaining oxygen vacancies. The absorption spectrum did not change after the additional annealing process, as shown in Fig. 4.2. The color of the post-annealed film was also identical to the as-deposited film, as can be seen in Fig. 4.3. This result indicates that the co-doping was indeed fully successful and the  $\text{Rh}^{3+}$  state could be stabilized without the need for oxygen vacancies. The absorption coefficient of the co-doped film was considerably higher than that of a film grown at low oxygen pressure. The reason for this is likely to be a larger amount of Rh incorporated in the film due to lower due to the suppression of evaporative loss of volatile Rh oxides at high process pressures.

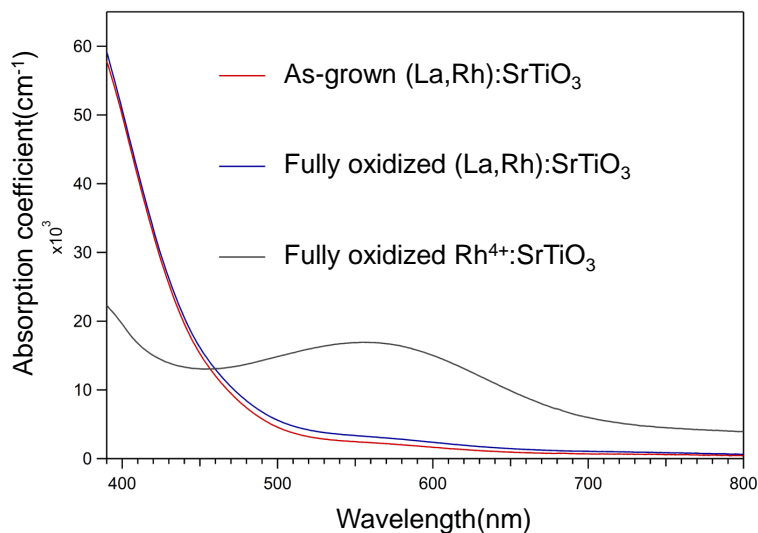


Figure 4.2: Absorption spectra of a  $(\text{La,Rh}):\text{SrTiO}_3$  film after growth at  $10^{-1}$  Torr and after post-annealing in air. The spectrum of a fully oxidized  $\text{Rh}^{4+}:\text{SrTiO}_3$  also shown for reference.

**(La,Rh):SrTiO<sub>3</sub>**

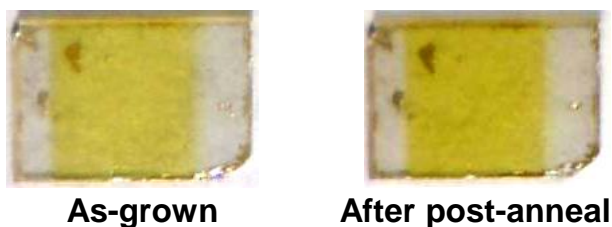


Figure 4.3: Pictures of a (La,Rh):SrTiO<sub>3</sub> film sample grown at  $10^{-1}$  Torr. The yellow color derived from the Rh<sup>3+</sup> dopant state is unchanged even after the as-grown (a) film was post-annealed in air (right).

The laser fluence was re-optimized for the co-doped films. The XRD  $2\theta/\theta$  scans are shown in Fig. 4.4 for several laser fluence values. Laser fluence above  $0.52 \text{ J/cm}^2$  was found to yield films with very nearly the expected bulk lattice parameter. However, slight lattice expansion was still observed. It is not possible to determine the reason for the slight lattice expansion from XRD analysis alone. Electron microscopy and photoelectron spectroscopy may offer clues as to the types of defects that may still be present in these films.



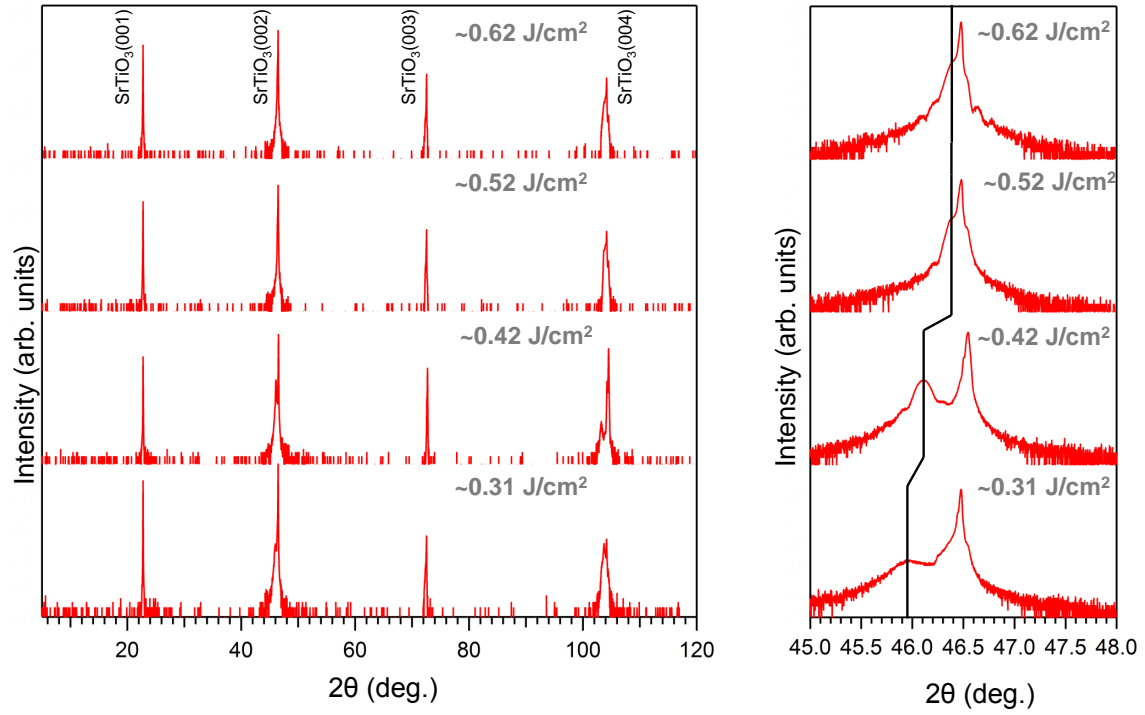


Figure 4.4: XRD  $2\theta/\theta$  scans of (La,Rh):SrTiO<sub>3</sub> films grown at various laser fluences on SrTiO<sub>3</sub> substrates at an oxygen pressure of  $10^{-1}$  Torr. The film thickness was 60 nm. Wide range scans show no misoriented phases. Narrow scans of the (002) peak show that lattice expansion is minimized by using a fluence above  $0.5 \text{ J/cm}^2$ .

## Chapter 5

### Photoelectrochemical activity

The Rh:SrTiO<sub>3</sub> and (La,Rh):SrTiO<sub>3</sub> films are both nominally *p*-type semiconductors with a very deep Fermi level. The resistivity of these films is too high to make an electrical contact from the edges of the film. Instead, a back electrode contact is necessary for electrochemical measurements. The most common back electrode would be a Nb-doped:SrTiO<sub>3</sub> substrate but since Nb:SrTiO<sub>3</sub> is an *n*-type material with a low work function of  $\sim 4.2$  eV, a Schottky-type junction would form between Nb:SrTiO<sub>3</sub> and Rh:SrTiO<sub>3</sub>. A lattice-matched bottom electrode is thus required for a uniform Ohmic back contact.

Therefore, Sr<sub>2</sub>RuO<sub>4</sub> films were grown on SrTiO<sub>3</sub>(001) substrates as bottom electrodes before Rh:SrTiO<sub>3</sub> or (Rh,La):SrTiO<sub>3</sub> film growth to form an Ohmic contact layer. Fig. 5.1(a) shows the Sr<sub>2</sub>RuO<sub>4</sub> crystal structure. Sr<sub>2</sub>RuO<sub>4</sub> has a tetragonal K<sub>2</sub>NiF<sub>4</sub>-type unit cell with the lattice constants  $a = 3.87$  Å and  $c = 12.74$  Å. [33, 34]). This material is well known as a copper-free and spin-triplet superconductor [35, 36] but at room temperature it is metallic and when looked along the *c* axis, has the same atomic layer structure as the perovskite lattice. Sr<sub>2</sub>RuO<sub>4</sub> therefore grows epitaxially on SrTiO<sub>3</sub> (100) substrate and can be used as a metallic layer between the perovskites SrTiO<sub>3</sub> substrate and the Rh:SrTiO<sub>3</sub> film. Sr<sub>2</sub>RuO<sub>4</sub> has been reported to form an Ohmic contact with Rh:SrTiO<sub>3</sub> and since both Rh:SrTiO<sub>3</sub> and (La,Rh):SrTiO<sub>3</sub> are *p*-type photocathodes, Sr<sub>2</sub>RuO<sub>4</sub> should also form an Ohmic contact with (La,Rh):SrTiO<sub>3</sub>. [8].

The Sr<sub>2</sub>RuO<sub>4</sub> thin films were grown from a SrRuO<sub>3</sub> target by PLD. One of the advantages of PLD is that the composition of the film very closely matches the deposition target material. However, for materials with significant vapor pressure, such as noble metal oxides, intentional composition change is sometimes possible. Sr<sub>2</sub>RuO<sub>4</sub> is one such case where the evaporative loss of Ru can be controlled by the deposition tem-

perature, forming a  $\text{Sr}_2\text{RuO}_4$  film from a  $\text{SrRuO}_3$  target. [37–39].  $\text{Sr}_2\text{RuO}_4$  films were grown at  $10^{-1}$  Torr of oxygen at  $900^\circ\text{C}$  and a laser fluence of  $0.47 \text{ J/cm}^2$ . An AFM image of a 30 nm thick  $\text{Sr}_2\text{RuO}_4$  film is shown in Fig. 5.1(b). A clear step-and-terrace structure is still visible, which means the  $\text{Sr}_2\text{RuO}_4$  layer is suitable as a bottom electrode for  $\text{Rh}:\text{SrTiO}_3$  film growth. The X-ray  $2\theta/\theta$  scans of an electrode film are shown in the Fig. 5.1(c). The  $\text{Sr}_2\text{RuO}_4$  is clearly  $c$ -axis oriented, showing only (00 $l$ ) reflections. An extra diffraction peak that appears at around  $44.5^\circ$  is related to imperfect stoichiometry control, but this does not affect the use of the film as an electrode. [40–42]

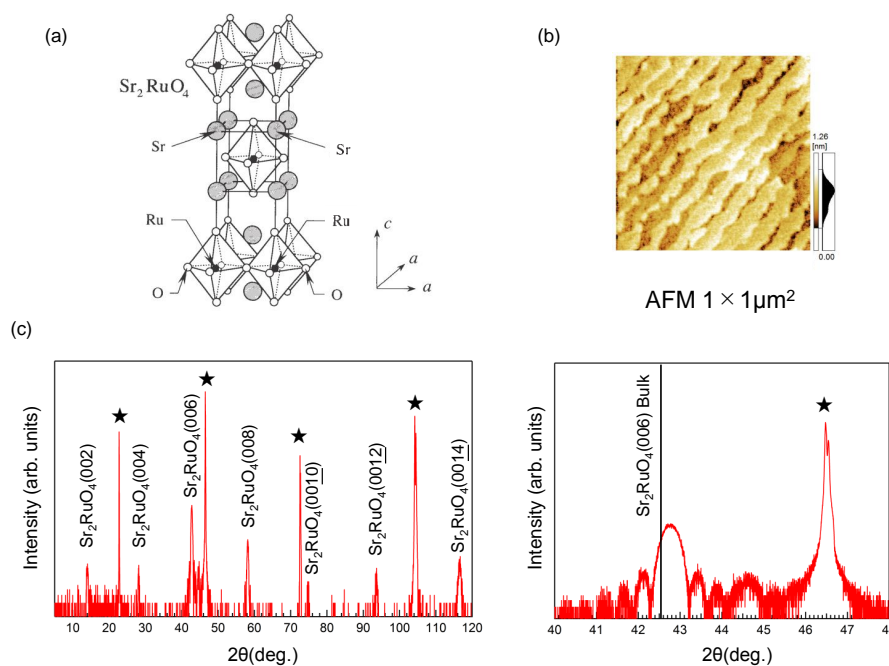


Figure 5.1: (a) Crystal structure ( $a = 3.87 \text{ \AA}$ ,  $c = 12.74 \text{ \AA}$ ) [35]. (b)  $1 \mu\text{m} \times 1 \mu\text{m}$  AFM image of the film surface. (c) XRD  $2\theta/\theta$  scans of a 30 nm thick  $\text{Sr}_2\text{RuO}_4$  film.

Electrochemical measurements were performed on 40 nm thick films of  $\text{Rh}^{3+}:\text{SrTiO}_3$  (with Rh clusters),  $\text{Rh}^{3+}:\text{SrTiO}_3$  (no clusters), and  $(\text{La,Rh}):\text{SrTiO}_3$  (co-doped). All films were grown on  $\text{Sr}_2\text{RuO}_4(16\text{nm})/\text{SrTiO}_3$  bottom electrodes. The clustered Rh and co-doped films were post-annealed in air to eliminate any volatile oxygen vacancies. The electrochemical measurements were done with a 0.1 M KOH (pH 13) electrolyte solution. Fig. 5.2 shows a comparison of cyclic voltammograms for these films under chopped visible light irradiation (400 ~ 720 nm). It is immediately clear from the plots that the co-doped film gave the largest photocurrent while the lowest current was

obtained in the clustered Rh film.

The photoresponse in the electrochemical cell is directly proportional to the number of generated photocarriers in the semiconductor. It is thus important to look at the absorption coefficients of the different films. The difference in the absorption rates of the non-clustered  $\text{Rh}^{3+}:\text{SrTiO}_3$  and co-doped  $(\text{La,Rh}):\text{SrTiO}_3$  films is small, but the electrochemical response is nearly three times higher. The absorption coefficient of the film that contains clustered Rh dopants shows a significantly lower absorption rate. This may be caused either by evaporative loss of  $\text{Rh}_2\text{O}_3$  during low-pressure deposition or the formation of metallic Rh clusters that do not dope the host  $\text{SrTiO}_3$  lattice.

The main difference between the cluster-free  $\text{Rh}^{3+}:\text{SrTiO}_3$  film and the co-doped film is the lack of oxygen vacancies in the co-doped  $(\text{La,Rh}):\text{SrTiO}_3$  film. Oxygen vacancies normally donate carriers to the  $\text{SrTiO}_3$  lattice. However, in vacancy-rich  $\text{Rh}^{3+}:\text{SrTiO}_{3-\delta}$  films these same oxygen vacancies can function as shallow photoelectron trap sites, reducing the carrier mobility and lifetime. This will have a direct negative impact on the photoelectrochemical activity.

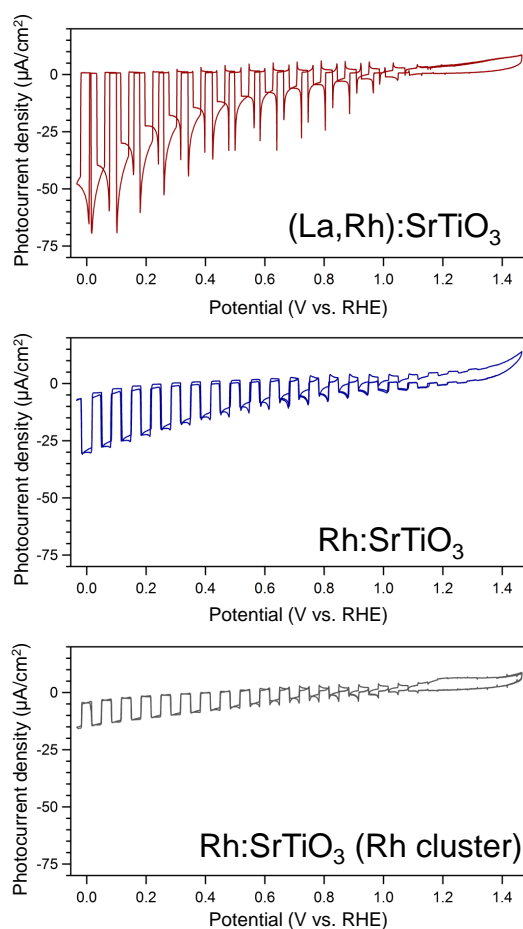


Figure 5.2: Cyclic voltammograms of three samples. Thickness of all films was 40 nm. Light source: chopped 100W Xe lamp with visible light module (400-720 nm). Electrolyte: 0.1 M KOH aq. (pH=13.0). Sweep rate: 20 mV/s.

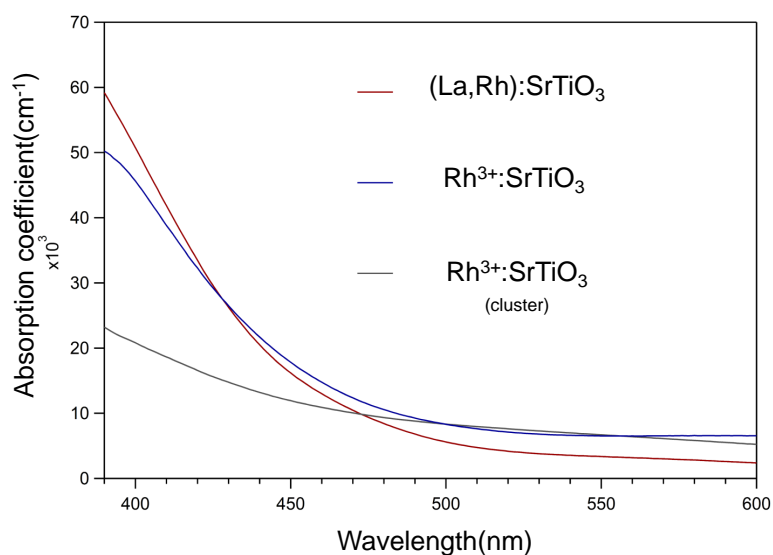


Figure 5.3: Absorption spectra of three samples used in electrochemical experiments.

The incident photon to current efficiency (IPCE) and the absorbed photon to current efficiency were calculated at 0 V vs. RHE. The results are shown Fig. 5.4 and Fig. 5.5. The IPCE plots shows clearly that the light absorption process is much more efficient in the co-doped film. The APCE plots show very little difference between the films where the Rh<sup>3+</sup> state was stabilized by oxygen vacancies. Regardless of whether Rh clustering occurs, the APCE values are almost the same. This shows that the Rh clusters themselves have little influence on the photoelectrochemical activity. The main issue for efficiency is the presence of oxygen vacancies in those films.

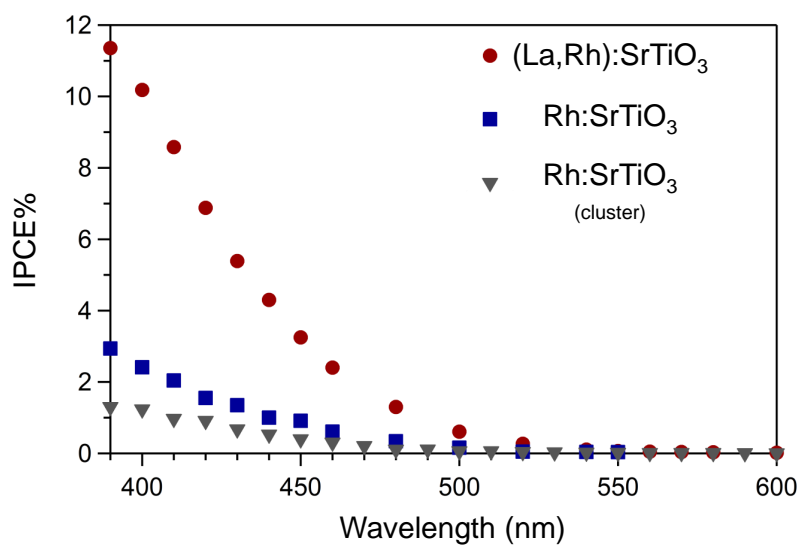


Figure 5.4: IPCE measured at 0 V vs. RHE. The light source was a 150W Xe lamp with a monochromator. Measured in a 0.1 M KOH aq. (pH = 13.0) solution.

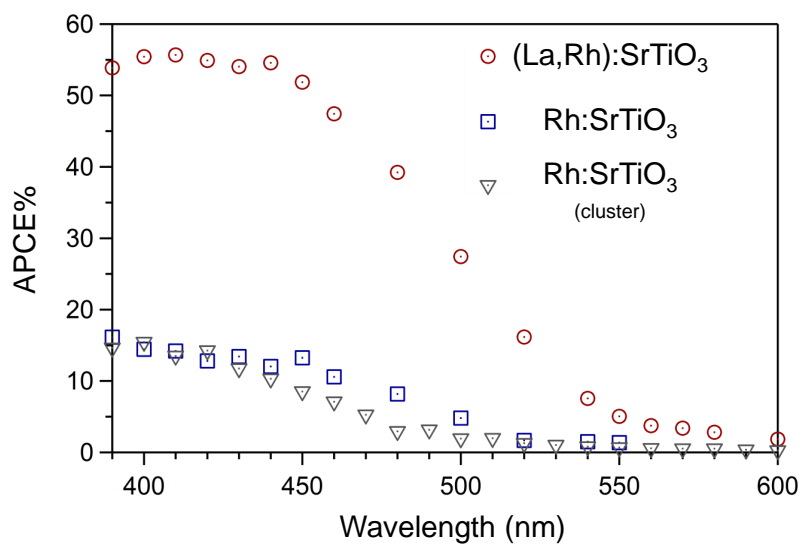


Figure 5.5: APCE plots as a function of wavelength. These plots were calculated from the IPCE results.

## Chapter 6

### Conclusions

Reducing the number of photocarrier-trapping defects in Rh:SrTiO<sub>3</sub> films was the topic of Chapter 3. The first attempt of fine-tuning the cation stoichiometry in Rh:SrTiO<sub>3</sub> films by adjusting the ablation laser fluence could reduce the lattice expansion in the films, and hence the number of point defects, ultimately the process optimization alone did not solve the problem of carrier trapping. In particular, the color of thin films with optimal cation stoichiometry remained unchanged after post-annealing. A Rh:SrTiO<sub>3</sub> film grown at reducing conditions contained predominantly Rh<sup>3+</sup> dopants, as shown by the yellow color of the film. However, this color did not change after an oxygen anneal, meaning that the valence state of Rh was set by other types of defects than randomly dispersed oxygen vacancies in the lattice.

The conclusion was that Rh:SrTiO<sub>3</sub> films grown at reducing conditions contain some types of Rh-related cluster defects that lead to a slight lattice expansion and fix the Rh valence at the 3+ state. For example, a cluster of two Rh atoms at neighboring lattice sites with an oxygen vacancy could lead to such behavior.

The second attempt to obtain a defect-free film was made by starting with a fully oxidized Rh<sup>4+</sup>:SrTiO<sub>3</sub> film grown at optimal laser fluence. The desired Rh<sup>3+</sup> state can be obtained by vacuum annealing but the lack of cation diffusion at the annealing temperature means that Rh clusters cannot form during the vacuum anneal process. Indeed, reversible film color change was achieved, showing that this strategy leads to a film with significantly lower density of defects. However, XPS analysis of a vacuum-annealed Rh<sup>3+</sup>:SrTiO<sub>3</sub> film showed that the surface of the film is oxidized back to the Rh<sup>4+</sup> state by exposure to ambient atmosphere. It thus became clear that it is impossible to stabilize the Rh<sup>3+</sup> valence state with oxygen stoichiometry control. Instead, a different doping scheme is required.



An additional important conclusion can be drawn from the absorption coefficient measurements of the two types of Rh:SrTiO<sub>3</sub> films. The absorption coefficient of the Rh<sup>3+</sup>:SrTiO<sub>3</sub> film grown at high oxygen pressure and then annealed in vacuum was much higher than that of a Rh<sup>3+</sup>:SrTiO<sub>3</sub> film grown directly at low pressure. This difference is apparently caused by volatilization of Rh at low absolute pressure growth. This means that the true Rh doping level of a film grown at low oxygen pressure is much lower than the Rh doping level of the ablation target.

The third strategy to stabilize the Rh<sup>3+</sup> state was discussed in Chapter 4. Oxygen vacancies in a SrTiO<sub>3</sub> lattice effectively donate two carriers that can convert a Rh<sup>4+</sup> dopants to the Rh<sup>3+</sup> state. Another way to introduce additional carriers into the lattice is to dope the Sr site with a trivalent ion, such as La. This idea was tested by growing (La,Rh):SrTiO<sub>3</sub> co-doped thin films. The films were grown in oxidizing conditions, at an oxygen pressure of 10<sup>-1</sup> Torr. Despite the oxidizing conditions, the film color was yellow, which indicates that the presence of La successfully stabilized the Rh<sup>3+</sup> state. Absorption spectra showed no presence of Rh<sup>4+</sup> in these films.

Despite the stoichiometry optimizations, the (La,Rh):SrTiO<sub>3</sub> films always exhibited a slight lattice expansion. Since the ionic radius of La is smaller than that of Sr, it is likely that the expanded lattice is due to lattice defects rather than the effect of La doping. As a lattice defect, an rocksalt-type SrO double layer defect can be considered. The films studied in this work were grown from Sr-rich targets to suppress Sr vacancy defects forming during high oxygen pressure growth. This Sr enrichment level was not specifically optimized, which means that the possibility of SrO defect layer formation cannot be ruled out.

Two methods are proposed for eliminating these defects. One possibility is to optimize further the film stoichiometry. Another possibility is to grow a stoichiometric thin film by changing the growth temperature. For comparison with previous studies, the co-doped (La,Rh):SrTiO<sub>3</sub> films were grown at 700°C. The optimal growth temperature may be different.

The results of the photoelectrochemical analysis of three types of films was described in Chapter 5. It was concluded from the quantum yield measurements that the presence of Rh-related clusters has little effect on carrier transport. The (La,Rh):SrTiO<sub>3</sub> films showed the highest electrochemical yield under visible light, but the yield was still low in absolute terms. A large optical absorption coefficient and high photocarrier mobility are indispensable for achieving higher energy conversion yields. Stronger absorption can, in principle, be achieved by higher doping, but this may decrease carrier

mobility. In other words, there is a trade-off between higher absorption and higher carrier mobility. Due to this, it is difficult to accomplish highly efficient water splitting with homogeneously-doped photoelectrodes. It may be possible to avoid this problem by using nanostructured photoelectrodes or heterojunction designs. For example, Cu(In,Ga)Se<sub>2</sub> (CIGS) is a photocathode material with a high absorption coefficient but low chemical stability. Attempts have been made to increase the stability of a CIGS electrode by depositing Pt-doped TiO<sub>2</sub> on a CIGS light absorber. As a result, the IPCE of the Pt:TiO<sub>2</sub>/CIGS photocathode exceeded 60% at -0.4 V vs RHE in the wavelength range of 400 ~ 800 nm [46]. Another advantage of heterojunctions is the promotion of charge separation. By doping BiVO<sub>4</sub> with W, the Fermi level rises slightly. Forming a heterojunction between non-doped BiVO<sub>4</sub> and W(1%):BiVO<sub>4</sub> enhances charge separation and photoelectrode activity. [47]

Improvement of photoelectrochemical characteristics by not only two-dimensional but also three-dimensional heterojunction has been reported. By controlling the growth condition of Ir:SrTiO<sub>3</sub>, Ir pillars can spontaneously form inside an Ir:SrTiO<sub>3</sub> film. Again, Schottky junctions form between Ir metal and Ir:SrTiO<sub>3</sub>, promoting charge separation and improving the photoelectrode efficiency. [48]. In conclusion, although co-doped (La,Rh):SrTiO<sub>3</sub> alone does not provide a high-efficiency electrode material, it may be possible to dramatically enhance the energy conversion efficiency by integrating (La,Rh):SrTiO<sub>3</sub> layers in suitable heterostructure designs.

# References

- [1] Chu, S. and Majumdar, Nature, 488, 294(2012)
- [2] A. Fujishima, K. Honda, Nature, 37, 238 (1972).
- [3] H. Gerischer, J. Electrochem. Soc., 113, 1174-1182 (1966).
- [4] J. M. Mavroides, J. A. Kafalas, and D. F. Kolesar, Appl. Phys. Lett. 28, 214 (1976)
- [5] M. Cardona, Phys. Rev. 140, A651 (1965).
- [6] A. Kudo and Y. Miseki, Chem. Soc. Rev., 2009, 38, 253
- [7] R. Konta, T. Ishii, H. Kato, and A. Kudo, J. Phys. Chem. B 108, 8992(2004).
- [8] S. Kawasaki, K. Nakatsuji, J. Yoshinobu, F. Komori, R. Takahashi, M. Lippmaa, K. Mase, and A. Kudo, Appl. Phys. Lett. 101, 033910 (2012).
- [9] S. Kawasaki, R. Takahashi, K. Akagi, J. Yoshinobu, F. Komori, K. Horiba, H. Kumigashira, K. Iwashina, A. Kudo, M. Lippmaa, J. Phys. Chem. C. 118, 20222 (2014)
- [10] T. Ohnishi, K. Shibuya, T. Yamamoto, and M. Lippmaa, J. Appl. Phys. 103, 103703 (2008).
- [11] Y. Tokuda, S. Kobayashi, T. Ohnishi, T. Mizoguchi, N. Shibata, Y. Ikuhara, and T. Yamamoto, Appl. Phys. Lett. 99, 033110 (2011).
- [12] Y. Kozuka, Y. Hikita, C. Bell, and H. Y. Hwang, Appl. Phys. Lett. 97, 012107 (2010)
- [13] T. Tanaka, K. Matsunaga, Y. Ikuhara, and T. Yamamoto, Phys. Rev. B 68, 205213 (2003).
- [14] S.Hasegawa, Char, Mater.(2012).

- [15] M.Lippmaa, N. Nakagawa, M. Kawasaki, S. Ohashi, and H. Koinuma, Appl. Phys, Lett. 76, 2439 (2000).
- [16] M. P. Seah and W. A. Dench, Surf. Interface Anal. 1, 2 (1979).
- [17] S. Kawasaki , K. Akagi , K. Nakatsuji , S. Yamamoto , I. Matsuda , Y. Harada , J. Yoshinobu , F. Komori , R. Takahashi , M. Lippmaa , C. Sakai , H. Niwa , M. Oshima , K. Iwashina , and A. Kudo , J. Phys. Chem. C 116, 24445 (2012).
- [18] M. Zimowska, J. B. Wagner, J. Dziedzic, J. Camra, B. Borzecka-Prokop, and M. Najbar, Chem. Phys. Lett., 417, 137 (2006).
- [19] Z. Weng-Sieh, R. Gronsky, and A. T. Bell, J. Catal., 170, 62 (1997).
- [20] M. Peuckert, Surf. Sci., 141, 500 (1984).
- [21] Y.-W. Chung and W.B.Weissbard, Phys. Rev. B, 20, 3456(1979).
- [22] G. M. Vanacore, L. F. Zagonel, and N. Barrett, Surf. Sci., 604, 1674 (2010).
- [23] R. Niishiro, H. Kato, and A. Kudo, Phys. Chem. Chem. Phys., 7, 2241 (2005)
- [24] H. Kato and A. Kudo, J. Phys. Chem. B, 106, 5029 (2002).
- [25] R. Niishiro, R. Konta, H. Kato, W.-J. Chun, K. Asakura, and A. Kudo, J. Phys. Chem. C, 111, 17420-17426 (2007).
- [26] W. Luo, Z. Li, X. Jiang, T. Yu, L. Liu, X. Chen, J. Yead, and Z. Zou, Phys. Chem. Chem. Phys., 10, 6717-6723 (2008).
- [27] K. Furuhashi, Q. Jia, A. Kudo and H. Onishi, J. Phys. Chem. C, 117, 19101 (2013).
- [28] R. Niishiro, S. Tanaka and A. Kudo, Appl. Catal. B, 150-151, 187 (2014).
- [29] R. Asai, H. Nemoto, Q. Jia, K. Saito, A. Iwase, and A. Kudo, Chem. Commun., 50, 2543 (2014).
- [30] P. Reunchan, S. Ouyang, N. Umezawa, H. Xu, Y. Zhang, and J. Ye, J. Mater. Chem. A, 1, 4221 (2013).
- [31] A. Kudo, R. Niishiro, A. Iwase, and H. Kato, Chem. Phys., 339, 104 (2007).

- [32] Wang, Q., Hisatomi, T., Ma, S., Li, Y. and Domen, K, Chem. Mater. 26, 41444150 (2014).
- [33] Randall, J. J. and Ward, R. J. Am. chem. Soc. 81, 26292631 (1959).
- [34] Lichtenberg, F., Catana, A., Mannhart, J. and Schlom, D. G. Appl. Phys. Lett. 60, 11381140 (1992).
- [35] Y. Maeno, H. Hashimoto, K. Yoshida, S. Nishizaki, T. Fujita, J. G. Bednorz and F. Lichtenberg Nature 372, 532 (1994)
- [36] K. Ishida, H. Mukuda, Y. Kitaoka, K. Asayama, Z. Q. Mao, Y. Mori and Y. Maeno, Nature 396, 658 (1998)
- [37] S. Ohashi, M. Lippmaa, N. Nakagawa, H. Nagasawa, H. Koinuma, and M. Kawasaki, Rev. Sci. Instrum. 70, 178 (1999).
- [38] T. Ohnishi and K. Takada, Appl. Phys. Express, 4, 025501 (2011)
- [39] R. Takahashi, M. Lippmaa, ACS Appl. Mater. Interfaces, 9, 21314(2017)
- [40] M. Uchida, M. Ide, H. Watanabe, K. S. Takahashi, Y. Tokura, and M. Kawasaki, APL Mater 5, 106108 (2017)
- [41] M. Vafaei, M. B. Yazdi, A. Radetinac, G. Cherkashinin, P. Komissinskiy, and L. Alff, J. Appl. Phys. 113, 053906 (2013).
- [42] M. Ito, M. Uchida, Y. Kozuka, K. S. Takahashi, and M. Kawasaki, Phys. Rev. B 93, 045139 (2016).
- [43] M. Markovich, J. Roqueta, J. Santiso, E. Lakin, E. Zolotoyabko, and A. Rothschild, Appl. Surf. Sci. 258, 9496 (2012).
- [44] D. A. Muller, N. Nakagawa, A. Ohtomo, J. L. Grazul, and H. Y. Hwang, Nature (London). 430, 657 (2004)
- [45] S. Kobayashi, Y. Mizumukai, T. Ohnishi, N. Shibata, Y. Ikuhara, and T. Yamamoto, ACS Nano 9, 10769 (2015).
- [46] Azarpira A, Lublow M, Steigert A, Bogdanoff P, Greiner D, Kaufmann CA, Kruger M, Gernert U, Krol Rvd, Fischer A, Schedel- Niedrig T. Adv Energy Mater 5, 1402148(2015)

- [47] F. F. Abdi, L. Han, A. H. M. Smets, M. Zeman, B. Dam and R. van de Krol, Nat. Commun, 4, 2195(2013)
- [48] S. Kawasaki, R. Takahashi, T. Yamamoto, M. Kobayashi, H. Kumigashira, J. Yoshinobu, F. Komori, A. Kudo and M. Lippmaa, Nat. Commun, 7, 11818(2016)

## Chapter 7

# Acknowledgement

I am deeply grateful to Prof. Mikk Lippmaa for his kindness, sincerity and politeness. He taught me a lot of things not just about science and research. The learning under him is a great wealth for me. I would like to express my deep appreciation to Doctor Ryota Takahashi. He supported not only research but also language. Without him this thesis can not exist. Prof. Kumigashira and their group was taken care of by XPS measurement. Mrs. Junko Kawamura made a great contribution in the administrative works. Mr, Xiuyi Hou gave me a lot of advice not only about experiment but also what is resarcher. Mr Naoyuki Osawa gave me much advice on the reseach and experimental techniques. A serious attitude toward his research changed my way of thinking. Mrs. Jiyon Lee's figure and poster design was very helpful for my presentation. Mr Katsuya Kihara made me fun in everyday life. The results of  $\text{Sr}_2\text{RuO}_4$  of Mr Kodai Ogawa helped me. I really appreciate Dr. Seiji Kawasaki. His advice and experimental data were essential in my research. I longed for him and chose this theme. That was the right choice. I tried to work hardly to overcome him everday. Of course, I couldn't beat him, however, I think that it was not a waste of effort for me. Finally, I deeply and deeply appreciate everyone involved in me.

*Yoshihisa Hosokawa*